Agricultural and Forest Meteorology 341 (2023) 109634

Contents lists available at ScienceDirect

Agricultural and Forest Meteorology

journal homepage: www.elsevier.com/locate/agrformet

Coupling a light use efficiency model with a machine learning-based water constraint for predicting grassland gross primary production

Ruiyang Yu [a], Yunjun Yao [a,*], Qingxin Tang [b], Changliang Shao [c,*], Joshua B. Fisher [d], Jiquan Chen [e], Kun Jia [a], Xiaotong Zhang [a], Yufu Li [f], Ke Shang [g], Junming Yang [a], Lu Liu [a], Xueyi Zhang [a,h], Xiaozheng Guo [a], Zijing Xie [a], Jing Ning [a], Jiahui Fan [a], Lilin Zhang [i]

[a] State Key Laboratory of Remote Sensing Science, Faculty of Geographical Science, Beijing Normal University, Beijing 100875, China
[b] School of Geography and Environment, Liaocheng University, Liaocheng 252000, China
[c] State Key Laboratory of Efficient Utilization of Arid and Semi-arid Arable Land in Northern China, National Hulunber Grassland Ecosystem Observation and Research Station, Institute of Agricultural Resources and Regional Planning, Chinese Academy of Agricultural Sciences, Beijing 100081, China
[d] Schmid College of Science and Technology, Chapman University, University Drive, Orange, CA 92866, USA
[e] Department of Geography, Environment, and Spatial Sciences, Michigan State University, East Lansing, MI 48823, USA
[f] Jincheng Meteorological Administration, Jincheng 048026, China
[g] School of Space Information, Space Engineering University, Beijing 101416, China
[h] Key Laboratory for Meteorological Disaster Monitoring and Early Warning and Risk Management of Characteristic Agriculture in Arid Regions, CMA, Yinchuan 750002, China
[i] Faculty of Geo-Information and Earth Observation (ITC), University of Twente, Enschede 7500 AE, The Netherlands

ARTICLE INFO

Keywords:
Gross primary production
Light use efficiency-gradient boosting regression trees
Grassland
Water constraint
Remote sensing

ABSTRACT

Light use efficiency (LUE) model was established to estimate gross primary production (GPP) for understanding the carbon-climate feedbacks of the terrestrial ecosystems. However, water constraints in LUE models can cause large uncertainties in GPP estimates, especially in semiarid grasslands where water is a key forcing factor for multiple ecosystem processes. Here, we proposed a novel LUE-Gradient Boosting Regression Trees (GBRT) model framework where water scalar is derived from five different water constraints for improving the estimates of grassland GPP over the conterminous United States (CONUS). The performance of LUE-GBRT and ten other GPP models [i.e., LUE-RF, LUE-ERT, GBRT, RF, ERT, LUE-f_{EF}, LUE-f_{VPD}, LUE-f_{LSWI}, LUE-f_{SM}, and LUE-f_{LST}] was evaluated against data from eddy covariance (EC) observations at 25 measurement sites over the CONUS domain from 2000 to 2021. We found that LUE-GBRT improved grassland GPP estimates at all EC sites and yielded the highest Kling-Gupta efficiency (0.85) and the lowest root-mean-square error (1.4 g C m^{-2} d^{-1}) when compared with the five individual GPP models. LUE-GBRT also showed a superior performance compared to LUE-RF and LUE-ERT. Compared with GBRT, the improvements were particularly from the responses to extreme surface conditions that were better characterized and estimated. An innovation of this method is that LUE-GBRT takes machine learning complementary to the physical-based LUE framework for an optimal junction between GPP physical process and model accuracy.

1. Introduction

Gross primary production (GPP) of terrestrial ecosystems, defined as the total amount of carbon dioxide (CO_2) absorbed by plants over a period (e.g., hour, day, year) through photosynthesis, is the largest carbon flux in the terrestrial carbon cycle (Odum et al., 1958). GPP plays a key role in maintaining the carbon-climate balance in the regional or global scale (Karlson et al., 2004). Grassland is an important component of terrestrial biomes because they account for twenty percent of global carbon reserves (Adams et al., 1990). In particular, grassland is a major ecosystem type over most of the western conterminous United States (CONUS) (UCMP 2022). Accurate estimation of grassland GPP is essential for understanding and quantifying the carbon budgets and carbon-climate feedbacks of CONUS.

Remote sensing technology has provided vegetation parameters with wide spatial coverage and regular temporal intervals (Norman et al.,

* Corresponding authors.
E-mail addresses: boyyunjun@163.com (Y. Yao), shaochangliang@caas.cn (C. Shao).

https://doi.org/10.1016/j.agrformet.2023.109634
Received 1 May 2023; Received in revised form 25 June 2023; Accepted 30 July 2023

1978; Townshend et al., 1985) for estimating regional grassland GPP. This is in contrast to complementary *in situ* eddy covariance (EC) observations that are location specific GPP. Due to the sparse distribution of EC towers, accurate estimation of regional GPP over the CONUS is quite limited. At present, remotely sensed GPP models include empirical, process-based and light use efficiency (LUE) models. The empirical models include linear and nonlinear approaches that are developed based on the statistical relationship between terrestrial GPP and climate variables, as well as satellite vegetation indices (Beer et al. 2010; Chen 2021). As classical nonlinear empirical approaches, machine learning (ML) methods have become important tools for GPP estimation (Chen 2023; Jung et al., 2009; Tramontana et al. 2016; Xiao et al. 2010; Yang et al. 2007). Previous studies have reported that many ML methods use satellite and meteorological data as input features to estimate GPP (Bai et al., 2021; Filippi et al., 2014; Wei et al., 2017; Yang et al. 2007). However, the empirical models lack rigorous physical mechanisms for the photosynthetic processes (Anav et al. 2015; Chen 2021). Process-based GPP models generally include detailed physical mechanisms (Chen et al., 1999; Ryu et al. 2011; Verrelst et al., 2016; Zhang et al., 2019). However, process-based GPP models usually require many parameters that often lead to large errors in GPP estimates (Chen 2023; Zhang et al., 2016).

Fortunately, the widely used satellite-based LUE models not only consider the response mechanism of photosynthetic efficiency to environmental conditions, but also have the potentials to simulate the temporal and spatial variation of plant growth at the regional scale with a few parameters, and even the global scale (Running et al., 2000). Water constraint is a main source of uncertainties for estimating the water-limited grassland GPP in the arid/semi-arid regions (Reichstein et al. 2002a). Previous studies found that the grassland GPP in the arid/semiarid regions was most sensitive to water stress (e.g., drought). Global GPP was reduced by 15% on average due to droughts as indicated by the soil moisture constraint, and the reduction in GPP was even higher by more than 50% in semiarid grasslands and savannahs (Stocker et al., 2019). Different LUE models have different metrics of water constraints for characterizing water stress for GPP estimates (Table 1). However, these models have different water constraints because water constraints of photosynthesis activity are influenced by many variables, including meteorological, soil moisture, vegetation water and surface energy variables. Various water constraints will cause large uncertainties in estimating grassland GPP and pose a serious obstacle to quantifying and understanding the global or regional carbon cycle (Beer et al. 2010). Clearly, it is required for improving the accuracy of grassland GPP estimates that a LUE model with the efficient water constraint (W_s) combines all available W_s information from regional and global satellite, hydrological and meteorological data.

Gradient Boosting Regression Trees (GBRT), a classical ML method, has provided an effective strategy to improve the model performance for estimating grassland GPP and LUE. For example, Bai et al. (2021) used GBRT approach method to quantify global GPP with different influencing factors and found GBRT performed best. However, this study estimated GPP directly from input variables and ignored the physical process of the LUE model driven by water constraints. We investigated the GBRT method for calculating W_s in the LUE model by combining satellite, meteorological and hydrological variables to estimate grassland GPP.

In this study, we developed a novel LUE-GBRT framework that coupled a LUE model with a ML-based W_s for estimating grassland GPP over the CONUS. Our objectives are to: (1) develop a novel LUE model by embedding a GBRT-based W_s for estimating grassland GPP; (2) assess the model performance of the LUE-GBRT based on ground measurements from 25 EC flux towers; and (3) implement the spatial distribution of grassland GPP using LUE-GBRT over the CONUS during 2019–2021.

Table 1
Summary of GPP LUE models with various water constraints. Descriptions of the abbreviations are in Table S1.

No.	Model Name	Equation	Water constraints	References
1	GLO-PEM	$GPP = PAR \times FPAR \times \varepsilon_{max} \times f_{SHD} \times f_{SM} \times T_s$	f_{SHD}, f_{SM}	(Prince and Goward 1995)
2	3-PG	$GPP = PAR \times FPAR \times \varepsilon_{max} \times min(f_{SM}, f_{VPD}) \times f_{SA} \times T_s$	f_{SM}, f_{VPD}	(Landsberg and Waring 1997)
3	MOD17	$GPP = PAR \times FPAR \times \varepsilon_{max} \times f_{VPD} \times f_{T_{min}}$	f_{VPD}	(Running et al., 2004)
4	VPM	$GPP = PAR \times FPAR \times \varepsilon_{max} \times f_{LSWI} \times f_P \times T_s$	f_{LSWI}	(Xiao et al., 2004)
5	CFLUX	$GPP = PAR \times FPAR \times [(\varepsilon_{\max} - \varepsilon_{cs}) \times f_{CI} + \varepsilon_{cs}] \times \min(f_{SM}, f_{VPD}) \times f_{SA} \times f_{T_{\min}}$	f_{SM}, f_{VPD}	(Turner et al., 2006)
6	LUE-type	$GPP = \varepsilon_{max} \times APAR \times f_{VPD} \times f_{SWC}$	f_{VPD}, f_{SWC}	(MÄKelÄ et al. 2008)
7	EC-LUE	$Version\ 1: GPP = PAR \times FPAR \times \varepsilon_{max} \times \min(T_s, f_{EF})$ $Version\ 2: GPP = PAR \times FPAR \times \varepsilon_{max} \times f_{CO_2} \times \min(T_s, f_{VPD})$	f_{EF}, f_{VPD}	(Yuan et al. 2007, 2010, 2019)
8	Horn's model	$GPP = \varepsilon_{max} \times [p \times T_s + (1 - p) \times f_{VPD}] \times APAR$	f_{VPD}	(Horn and Schulz 2011)
9	TL-LUE	$GPP = (APAR_{su} \times \varepsilon_{msu} + APAR_{sh} \times \varepsilon_{msh}) \times f_{VPD} \times T_s$	f_{VPD}	(He et al. 2013)
10	PCM	$GPP = PC_{max} \times f_{EVI} \times f_{LSWI}$	f_{LSWI}	(Gao et al. 2014)
11	TL-LUE$_n$	$GPP = ((APAR_{su} \times \varepsilon_m \times \tau) / (APAR_{su} \times \varepsilon_m + \tau) \times LAI_{su} + (APAR_{sh} \times \varepsilon_m \times \tau) / (APAR_{sh} \times \varepsilon_m + \tau) \times LAI_{sh}) \times f_{VPD} \times T_s$	f_{VPD}	(Wu et al. 2015)
12	TEC	$GPP = PAR \times FPAR \times \varepsilon_{max} \times f_E \times T_s$	f_E	(Yan et al., 2015)
13	MVPM	$GPP = PAR \times FPAR \times \varepsilon_{max} \times min(f_{LSWI} \times f_{VPD}, T_s)$	f_{LSWI}, f_{VPD}	(Zhang et al., 2015a)
14	CI-LUE	$GPP = PAR \times FPAR \times [(\varepsilon_{max} - \varepsilon_{cs}) \times f_{CI} + \varepsilon_{cs}] \times f_{VPD} \times T_s$	f_{VPD}	(Wang et al. 2015)
15	MuSyQ	$GPP = PAR \times FPAR \times \varepsilon_{max} \times f_E \times T_s$	f_E	(Cui et al., 2016)
16	CCW	$GPP_{or} = PAR \times FPAR \times \varepsilon_{max} \times f_{CI} \times \min(f_{VPD}, T_s)$ $GPP_{and} = PAR \times FPAR \times \varepsilon_{max} \times f_{CI} \times f_{VPD} \times T_s$	f_{VPD}	(Zhang et al., 2016)
17	TCF	$GPP = PAR \times FPAR \times \varepsilon_{max} \times f_{VPD} \times f_{SM} \times f_{FT} \times T_s$	f_{VPD}, f_{SM}	(He et al., 2016)
18	DTEC	$GPP = (APAR_{su} \times \varepsilon_{msu} + APAR_{sh} \times \varepsilon_{msh}) \times f_E \times T_s$	f_E	(Yan et al. 2017)
19	Wang's model	$GPP = PAR \times FPAR \times \varepsilon_{max} \times f_{PM} \times f_{VPD} \times f_{SWC} \times (1 - \mu \times f_{CI}) \times T_s$	f_{VPD}, f_{SWC}	(Wang et al., 2018a)
20	CI-EF	$GPP = PAR \times FPAR \times [\varepsilon_{cs} + (\varepsilon_{max} - \varepsilon_{cs}) \times f_{CI}] \times f_{EF} \times f_{T_{min}}$	f_{EF}	(de Almeida et al. 2018)
21	PRELES	$GPP = \varepsilon_{max} \times APAR \times f_L \times T_s \times f_{VPD} \times f_{SWC}$	f_{VPD}, f_{SWC}	(Kalliokoski et al., 2018)
22	P-model V1.0	$GPP = PAR \times FPAR \times m' \times M_C \times T_s \times f_{SM}$	f_{SM}	(Stocker et al., 2020)
23	TL model	$GPP = (APAR_{su} \times \varepsilon_{msu} + APAR_{sh} \times \varepsilon_{msh}) \times T_s \times f_{VPD} \times f_{SM} \times f_L$	f_{VPD}, f_{SM}	(Bao et al., 2022a)
24	BL model	$GPP = APAR \times \varepsilon_{max} \times T_s \times f_{VPD} \times f_{SM} \times f_L \times f_{CI}$	f_{VPD}, f_{SM}	(Bao et al. 2022b)
25	CASA	$GPP = PAR \times FPAR \times \varepsilon_{max} \times T_s \times f_E$	f_E	(Potter et al., 1993)

2. LUE-GBRT

2.1. LUE-GBRT framework

The LUE-GBRT framework contains two modules: a LUE host model and a GBRT-based W_s module embedded in the host model (Fig. 1).

The LUE host model has six components: photosynthetically active

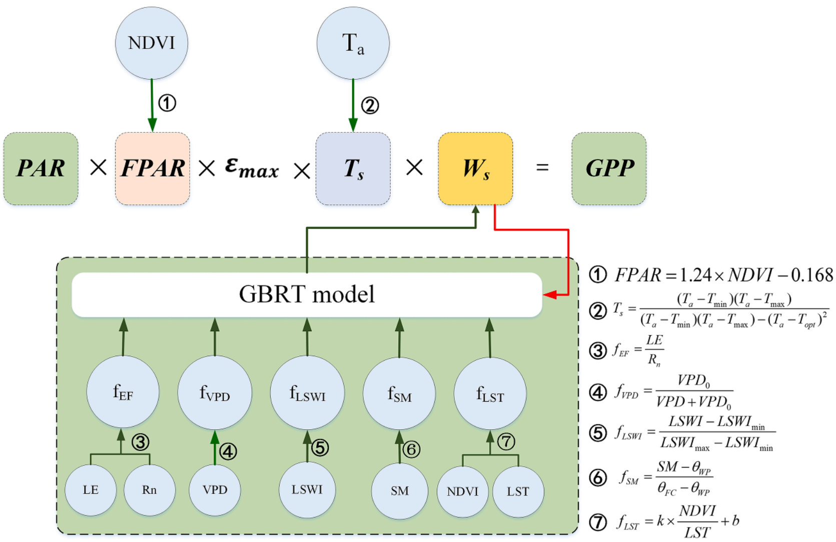

Fig. 1. Model framework of Light Use Efficiency-Gradient Boosting Regression Trees (LUE-GBRT) by coupling various water constraints for gross primary production (GPP) estimates. PAR is the photosynthetically active radiation (MJ m^{-2} d^{-1}). FPAR is the fraction of PAR absorbed by the vegetation. NDVI is normalized difference vegetation index. ε_{max} is maximum LUE. T_s is air temperature (T_a) constraint. T_{max}, T_{min}, and T_{opt} are maximum, minimum, and optimum T_a (°C), respectively. W_s is water constraint of LUE model. f_{EF}, f_{VPD}, f_{LSWI}, f_{SM} and f_{LST} are W_s equations of evaporative fraction (EF), vapor pressure deficit (VPD, kPa), land surface water index (LSWI), soil moisture (SM, m^3/m^3) and land surface temperature (LST, K), respectively. LE is the latent heat flux, and R_n is net radiation (W/m^2). VPD_0 is the parameter of f_{VPD}. $LSWI_{min}$ and $LSWI_{max}$ are the minimum and maximum LSWI, respectively. θ_{FC} and θ_{WP} are the field capacity and volumetric soil water permanent wilting point, respectively. *k* and *b* are the coefficients of f_{LST}, respectively. The red arrow indicates that the inversion W_s derived from EC-based GPP is added in the GBRT model as the target variable, and the green arrow represents that W_s estimates derived from GBRT model are added in the host LUE model.

radiation (PAR, MJ m^{-2} d^{-1}), fraction of PAR absorbed by the vegetation (FPAR), maximum LUE (ε_{max}, 2.14 g C m^{-2} MJ^{-1}), air temperature constraint (T_s), W_s, and GPP (Myneni and Williams 1994; Yuan et al. 2007):

$$GPP = PAR \times FPAR \times \varepsilon_{max} \times T_s \times W_s \tag{1}$$

$$FPAR = 1.24 \times NDVI - 0.168 \tag{2}$$

$$T_s = \frac{(T_a - T_{min})(T_a - T_{max})}{(T_a - T_{min})(T_a - T_{max}) - (T_a - T_{opt})^2} \tag{3}$$

where T_s varies between 0 and 1, as well as W_s. T_{opt}, T_{max}, and T_{min} are the optimum (20.33 °C), maximum (40 °C), and minimum (0 °C) air temperatures for photosynthesis, respectively (Raich et al., 1991).

2.2. Water constraints in the LUE model

Considering that EF, VPD, LSWI, SM and LST all influence the water variations in grassland GPP, five water constraints (f_{EF}, f_{VPD}, f_{LSWI}, f_{SM} and f_{LST}) were included to predict the W_s of the LUE models. f_{EF}. f_{EF} represents the surface dryness that R_n can be divided into sensible heat flux (H) and LE (Lewis 1995). f_{EF} can be expressed as (Yuan et al. 2010):

$$f_{EF} = \frac{LE}{R_n} (0 < f_{EF} < 1) \tag{4}$$

f_{VPD} refers to the atmospheric dryness above the canopy and indirectly characterizes the W_s of the LUE model for estimating grassland GPP (Yuan et al. 2019).

$$f_{VPD} = \frac{VPD_0}{VPD + VPD_0} (0 < f_{VPD} < 1) \tag{5}$$

where VPD_0 was calibrated using GPP observations at EC towers and was optimized as 1.703 kPa. f_{LSWI} can show the water content of soil and plants in liquid (Chen et al., 2005). It can be expressed as (Zhang et al., 2021):

$$f_{LSWI} = \frac{LSWI - LSWI_{min}}{LSWI_{max} - LSWI_{min}} (0 < f_{LSWI} < 1) \tag{6}$$

where $LSWI_{min}$ and $LSWI_{max}$ are the minimum and maximum LSWI values from the reflectance products corresponding to the flux sites during the growing seasons. f_{SM} is the most direct tool to represent the control of soil on W_s from surface extractable water (Jin et al., 2011). It can be expressed as (Purdy et al., 2018):

$$f_{SM} = \frac{SM - \theta_{WP}}{\theta_{FC} - \theta_{WP}} (0 < f_{SM} < 1) \tag{7}$$

where θ_{WP} and θ_{FC} are the volumetric soil water permanent wilting point (at soil water potential of 1500 kPa, m^3 m^{-3}) and field capacity (at soil water potential of 33 kPa, m^3 m^{-3}), respectively. θ_{WP} and θ_{FC} of each site were extracted from a global soil dataset for earth system modeling (~10 km × 10 km) (Shangguan and Dai 2014; Shangguan et al., 2014). We obtained θ_{WP} and θ_{FC} by averaging the values in the upper soil layers from 0 to 0.29 m (Zhang et al., 2015b). f_{LST} combines NDVI and LST, which are related to the LE (Jiang and Islam 1999).

$$f_{LST} = k \times \frac{NDVI}{LST} + b (0 < f_{LST} < 1) \tag{8}$$

where *k* and *b* are optimized as 121.36 and 0.34, respectively.

2.3. Machine learning methods for Ws estimation

W_s was estimated using ML methods by establishing the functional relationships between the inversion W_s and the corresponding five W_s equations (f_{EF}, f_{VPD}, f_{LSWI}, f_{SM} and f_{LST}). In this study, we calculated the W_s by GBRT and compared it with random forests (RF) and extremely randomized trees (ERT).

GBRT, a widely used ML algorithm (Friedman 2001), is an ensemble learning method which combines multiple trees to build a regression model. It is of competitive, highly stable, explainable routines for regression to mine redundant data (Fig. 2).

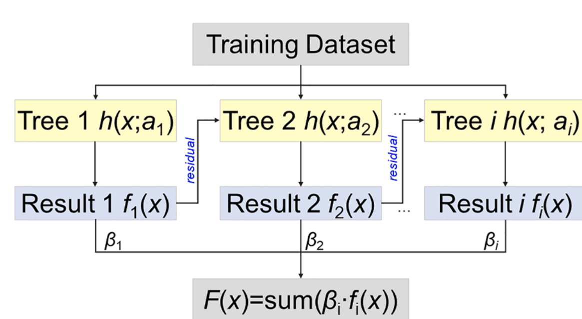

Fig. 2. Diagram of the GBRT algorithm. The training samples are brought into regression trees [$h(x; a_i)$] and calculated to obtain the results [$f_i(x)$] through the weight regression. β_i is the weight of the i^{th} tree. $F(x)$ is the sum of the weighted regression results.

GBRT can be described as:

$$F(x) = \sum_{i=1}^{N} \beta_i h(x; a_i) \quad (9)$$

where x refers to the argument, and a_i represents the regressor of each regression tree. Every tree is defined as $h(x; a_i)$. β_i refers to the weight of the i^{th} tree, and N is the total number of regression trees. In GBRT model, the thin learner judges the errors in every node and uses the test function to separate the nodes. The GBRT model is able to reduce the biases and better than other tree-based algorithms for overfitting as well as cost calculation, because all the regression trees are mutually connected, and the major virtue lies in that the regression tree of the GBRT is fitted based on the surplus of the preceding tree (Friedman 2001). In addition, GBRT has the advantages of relating the capacity to solve the heterogeneous distribution of data attributes and no limitations on any hypothesis of input variables. Regardless of its copositive algorithm, GBRT has better estimation ability and robustness than those of the single decision tree.

Several machine learning methods are applied, including:

RF is an integration of tree estimators where each tree is of a random vector sampled by itself distributing in the same way for all forest trees as similar with the GBRT algorithm (Breiman 2001). The tree of RF is calibrated in parallel while that of GBRT not. The single tree predictor in the entirety is produced by choosing arguments with the bootstrap method randomly (Chatterjee and Lahiri 2011). When coming into being decision trees may disintegrate predicted errors, the randomization appended to the forests. RF means can remove these errors (Xu et al. 2018).

ERT is a supervised method of regression similar with the RF (Geurts et al., 2006). It is an ensemble ML method based on tree predictors and made up of stochastic properties and breaks choices while a tree node is separated. Under extreme conditions, the trees are established randomly in structure with independent results. From many regression trees, ERT obtains its results averaging the outputs. These trees are calibrated by dividing the origin dataset into subset and following simple rules from the parameter information (Geurts et al., 2006).

2.4. Our experiments

The LUE-GBRT is a LUE framework that integrates the multiple water constraints based on ML methods (Fig. 1). The experimental procedure contains four steps. Firstly, to build the LUE-GBRT, we selected PAR, NDVI, T_a, LE, R_n, VPD, SM, LSWI, LST, GPP observations and the corresponding inversion daily W_s using the following Eq. (10) at the EC flux sites.

$$W_s = \frac{GPP}{PAR \times FPAR \times \varepsilon_{\max} \times T_s} (0 < W_s < 1) \quad (10)$$

Secondly, we used all 25 EC flux sites to evaluate the LUE-ML models by leave-one-out cross-validation. The water constraints (f_{EF}, f_{VPD}, f_{LSWI}, f_{SM} and f_{LST}) were indicated as the input features for the GBRT model, and two other machine learning methods (i.e., RF and ERT), and the inversion daily W_s was indicated as a target variable, which is referred to as Eq. (11):

$$W_s \sim ML(f_{EF}, f_{VPD}, f_{LSWI}, f_{SM}, f_{LST}) \quad (11)$$

In addition, we simulate grassland GPP by pure ML methods to compare with the LUE-ML model:

$$GPP \sim ML(PAR, FPAR, T_s, f_{EF}, f_{VPD}, f_{LSWI}, f_{SM}, f_{LST}) \quad (12)$$

where PAR, FPAR, T_s, f_{EF}, f_{VPD}, f_{LSWI}, f_{SM} and f_{LST} were used as input variables, and the GPP observations were used as the target variable in Eq. (12). We built the GBRT, RF and ERT with sklearn modules of Python and used the GridSearchCV module to find the best parameters for each model. For models established with sklearn modules, the most vital parameters are n_estimator, max_depth and max_features, which affect the extent of overfitting. Typically, parameter max_features equal N or $\log_2 N$ (N represents the number of input variables). The GridSearchCV module tunes the parameters by trying each possibility among all parameter combinations through loop traversal and then choosing the optimal ones. We evaluated the performance of ML model using leave-one-out cross-validation (Xiao et al. 2010), i.e., data from every site was applied for validation, after the remaining sites provided samples for the training of the ML models. Training and testing data were independent. The leave-one-out cross-validation was conducted for all sites, respectively. The optimal model parameters with the highest correlation coefficient were chosen, and applied to estimate the W_s. Thirdly, we used PAR, FPAR, ε_{max}, T_s and W_s estimates to simulate grassland GPP by the LUE model. Finally, we generated 8-day grassland GPP products with 1 km spatial resolution over the CONUS during 2019–2021.

2.5. Model evaluation

2.5.1. Validation metrics

To evaluate the capacity of different models, we used the Kling-Gupta efficiency (KGE), bias, root-mean-square error (RMSE) and coefficient of determination (R^2). KGE, a comprehensive metric, couples the mean value ratio (γ), correlation (r), and relative variability ratio (α) (Gupta et al., 2009). Under the condition with no estimation errors, the ideal values are $r=\alpha=\gamma=1$. Therefore, the best value of KGE is 1.

2.5.2. ML model interpretability analysis

SHAP (SHapley Additive exPlanations) (Lipovetsky and Conklin 2001) values are applied to predict the contribution of each constraint to LUE-GBRT. The Shapley interaction index derived from game theory turns into SHAP values (Fujimoto et al., 2006), which interpret estimates as total of actual contribution values of each argument (Lundberg et al., 2018). The feature j of a sample (x_i) is x_{ij}. The estimate of the model for x_i is y_i, and the model baseline estimates (i.e., the average value of the dependent variables of the whole samples) is y_0. It can be expressed as:

$$y_i = y_0 + f(x_{i1}) + f(x_{i2}) + \ldots + f(x_{ij}) \quad (13)$$

where $f(x_{ij})$ is the Shapley value of x_{ij}. The calculation of SHAP value is processed by Python.

3. Data and variables derivation

3.1. Data at EC flux tower sites

We used meteorological and eddy covariance (EC) data of 25 grassland sites collected from AmeriFlux (https://ameriflux.lbl.gov) and FLUXNET (https://fluxnet.org)(Table 2, Fig. 3). The data in 17 AmeriFlux sites included half-hourly or hourly net ecosystem exchange (NEE), soil temperature (T_{soil}) and water content (SWC), resulting in a total of 129 site-years of measurements. If more than a quarter of the data were missing on a specific day, the value of that day was considered missing. We estimated daily EC-based GPP using T_{soil}, SWC and NEE according to the approach of Reichstein et al. (2003). Ecosystem respiration (R_e) was related to T_{soil} and SWC through the regression model described by Reichstein et al. (2002b). We used T_{soil} and SWC data to estimate R_e, and then obtained GPP according to GPP = R_e-NEE. We directly used daily GPP data from eight FLUXNET grassland sites with a total of 46 site-years of measurements. Each site of AmeriFlux and FLUXNET included at least sequential one year data.

3.2. Satellite and reanalysis datasets

We used the 8-day 500 m surface reflectance product (MOD09A1) of

Table 2
Summary of 25 AmeriFlux and FLUXNET grassland EC sites over the CONUS, including the site code, name, latitude (°N), longitude (°W), mean annual temperature (MAT, °C), mean annual precipitation (MAP, mm), elevation (m), climate type, start year, end year and references. * Climate Type is the Köppen-Geiger class (Beck et al., 2020). Cfb: Temperate, no dry season, warm summer; Csb: Temperate, dry summer, warm summer; Cfa: Temperate, no dry season, hot summer; Dfa: Cold, no dry season, hot summer; Dsa: Dry continental, hot summer; Dsb: Cold, dry summer, warm summer; Csa: Temperate, dry summer, hot summer; Bsk: Arid, steppe, cold; Bwh: Arid, desert, hot.

Site Code	Site Name	Latitude (°N), longitude (°W)	MAT (°C)	MAP (mm)	Elevation (m)	Climate Type*	Start year	End year	Project	References
US-A32	ARM-SGP Medford hay pasture	36.82, 97.82	33.90	889	335	Cfa	2015	2017	AmeriFlux	(Dave et al., 2018)
US-AR1	ARM USDA UNL OSU Woodward Switchgrass 1	36.43, 99.42	–	–	611	Dsa	2009	2012	FLUXNET	(Dave et al., 2019a)
US-AR2	ARM USDA UNL OSU Woodward Switchgrass 2	36.64, 99.60	–	–	646	Dsa	2009	2012	FLUXNET	(Dave et al., 2019b)
US-ARb	ARM Southern Great Plains burn site-Lamont	35.550, 98.040	–	–	424	Cfa	2005	2006	FLUXNET	(Margaret 2019a)
US-ARc	ARM Southern Great Plains control site-Lamont	35.547, 98.040	–	–	424	Cfa	2005	2006	FLUXNET	(Margaret 2019b)
US-Aud	Audubon Research Ranch	31.59, 110.51	14.85	438	1469	Bsk	2002	2011	AmeriFlux	(Tilden 2016a)
US-CaV	Canaan Valley	39.06, 79.42	7.97	1317	994	Cfb	2004	2010	AmeriFlux	(Tilden 2016b)
US-Cop	Corral Pocket	38.09, 109.39	–	–	1520	–	2001	2007	AmeriFlux	(David 2019)
US-Dia	Diablo	37.68, 121.53	15.60	265	323	Csa	2010	2012	AmeriFlux	(Sonia 2016)
US-Fwf	Flagstaff-Wildfire	35.45, 111.77	8.40	557	2270	Csb	2005	2010	AmeriFlux	(Sabina and Thomas 2019)
US-Goo	Goodwin Creek	34.25, 89.87	15.89	1426	87	Cfa	2002	2006	FLUXNET	(Tilden 2019)
US-IB2	Fermi National Accelerator Laboratory- Batavia (Prairie site)	41.84, 88.24	9.04	930	227	Dfa	2004	2014	FLUXNET	(Roser 2019)
US-KFS	Kansas Field Station	39.06, 95.19	12.00	1014	310	Cfa	2007	2019	AmeriFlux	(Nathaniel 2020a)
US-KLS	Kansas Land Institute	38.77, 97.57	12.00	812	373	Cfa	2012	2019	AmeriFlux	(Nathaniel 2021)
US-Kon	Konza Prairie LTER (KNZ)	39.08, 96.56	12.77	867	417	Cfa	2008	2019	AmeriFlux	(Nathaniel 2020b)
US-KUT	KUOM Turfgrass Field	44.99, 93.19	7.90	777	301	Dfa	2005	2009	AmeriFlux	(Joe 2016)
US-LS1	San Pedro River Lewis Springs Sacaton Grassland	31.56, 110.14	17.00	288	1230	Bwh	2003	2007	AmeriFlux	(Russell 2020)
US-Ro4	Rosemount Prairie	44.68, 93.07	6.40	879	274	Dfa	2014	2021	AmeriFlux	(John and Tim 2022)
US-SdH	Nebraska SandHills Dry Valley	42.07, 101.41	–	–	1081	Dsb	2004	2009	AmeriFlux	(Dave and Tim 2016)
US-Snd	Sherman Island	38.037, 121.754	15.60	358	−5	Csa	2007	2014	AmeriFlux	(Matteo et al., 2016)
US-Sne	Sherman Island Restored Wetland	38.037 ,121.755	16.09	311	−5	Csa	2016	2020	AmeriFlux	(Robert et al., 2021)
US-Snf	Sherman Barn	38.04, 121.73	–	–	−4	Csa	2018	2019	AmeriFlux	(Kuno et al., 2020)
US-SRG	Santa Rita Grassland	31.79, 110.83	17.00	420	1291	Bsk	2008	2014	FLUXNET	(Russell 2023a)
US-Var	Vaira Ranch-Ione	38.41, 120.95	15.80	559	129	Csa	2000	2020	AmeriFlux	(Ma et al., 2022)
US-Wkg	Walnut Gulch Kendall Grasslands	31.74, 109.94	15.64	407	1531	Bsk	2004	2014	FLUXNET	(Russell 2023b)

Moderate Resolution Imaging Spectroradiometer (MODIS) (https://appeears.earthdatacloud.nasa.gov). We extracted the 8-day values corresponding to the EC sites for NDVI and LSWI. We linearly interpolated daily values from the 8-day composite values, and resampled the image data of NDVI and LSWI from 500 m to 1 km spatial resolution using a simple average method. We also directly used the land cover data (MCD12Q1) with a 500 m spatial resolution to extract the grassland over the CONUS.

We used the SM product V07.1 from European Space Agency (ESA) Climate Change Initiative (CCI) website (https://www.esa-soilmoisture-cci.org) (Dorigo et al. 2017; Gruber et al., 2019). The daily values were extracted from the pixels of SM product corresponding to the EC sites. The daily SM was downscaled from 25 km to 1 km in bilinear interpolation.

We also used T_{max} (°C), T_{min} (°C), daily actual vapor pressure (e, pa), daytime incident shortwave radiation (R_s, W/m^2), and the duration of the daylight period (dayl, s/day) from Daily Surface Weather and Climatological Summaries Version 4 (DAYMET V4, https://daac.ornl.gov) with a 1 km spatial resolution (Thornton et al., 2020). The daily values were extracted from the pixels covering the EC sites.

Considering that there was no satellite-derived all-sky hourly LST product available over the CONUS, we employed all-sky instantaneous LST product from the North American Land Data Assimilation System (NLDAS) (Xia et al. 2012). We used the 21:00 (UTC) instantaneous LST (NLDAS NOAH0125_H002) product with a 0.125° spatial resolution from the NLDAS Noah model (https://disk.gsfc.nasa.gov). The instantaneous values were extracted at the pixels where the EC sites are located. We downscaled the LST product to 0.01° in bilinear interpolation.

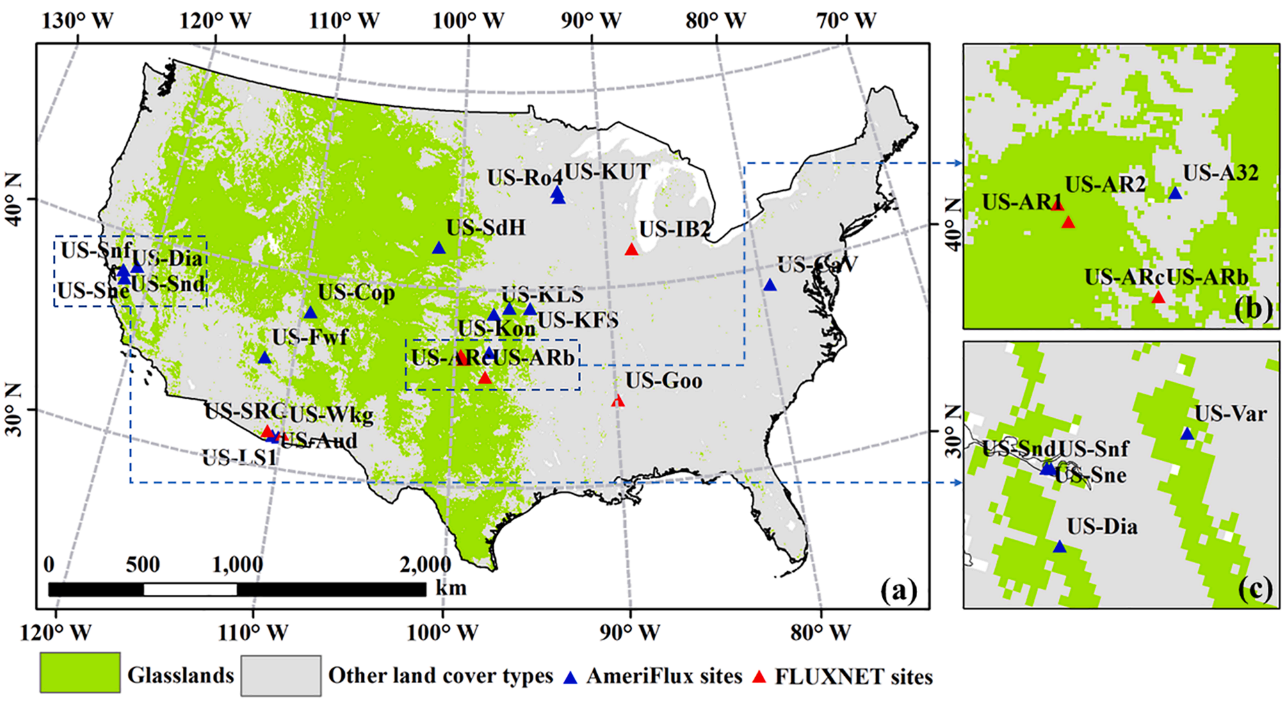

Fig. 3. Study domain. (a) The spatial distribution of grasslands, other land cover types and 25 grassland EC sites over the CONUS; (b) and (c) are the regional magnifications of the places where the EC sites are dense.

3.3. Variable derivation

Because the ratio of the PAR and total incident solar energy is approximately 0.48 (Frouin and Pinker 1995), the PAR was calculated as follows:

$$PAR = 0.48 \times R_s \times dayl \times 10^{-6} \tag{14}$$

We used the method proposed by Liang (2001) to calculate the albedo (θ), and R_n was calculated by the method developed by Jiang et al. (2015).

$$\theta = 0.160 \times \theta_1 + 0.291 \times \theta_2 + 0.243 \times \theta_3 + 0.116 \times \theta_4 + 0.112 \times \theta_5 + 0.081 \times \theta_7 - 0.0015 \tag{15}$$

$$R_n = R_s \times (1-\theta) \times (0.5515 + 0.0027 \times T_{\min} + 0.0015 \times DT + 0.1321 \times NDVI + 0.1652 \times RH) - 10.7575 \tag{16}$$

where $\theta_{1\text{–}5,7}$ refers to the MODIS reflectance from bands 1–5, and 7. DT and RH are the diurnal temperature range (°C) and air relative humidity, respectively.

We also used the modified satellite-based Priestley-Taylor algorithm (MS-PT) to estimate daily LE (Yao et al. 2013). MS-PT is a DT range modification of the PT-JPL LE model (Fisher et al., 2008). LE includes canopy transpiration (LE_{can}), canopy interception evaporation (LE_{ican}), saturated wet (LE_{ws}) and unsaturated soil evaporation (LE_s). It can be expressed as:

$$LE = LE_s + LE_{can} + LE_{ican} + LE_{ws} \tag{17}$$

$$LE_s = (1 - f_{wet}) f_{SM} a \frac{\Delta}{\Delta + \gamma} (R_{nsoil} - G) \tag{18}$$

$$LE_{can} = (1 - f_{wet}) f_{vc} T_s a \frac{\Delta}{\Delta + \gamma} R_{nvc} \tag{19}$$

$$LE_{ican} = f_{wet} a \frac{\Delta}{\Delta + \gamma} R_{nvc} \tag{20}$$

$$LE_{wsoil} = f_{wet} a \frac{\Delta}{\Delta + \gamma} (R_{nsoil} - G) \tag{21}$$

where a is the Priestly Taylor coefficient and γ is the psychrometric constant. $\triangle$ is the slope of the saturation e versus T_a. f_{wet} is the relative land wetness. DT_{max} describes the maximum DT. G, R_{nvc}, and R_{nsoil} are the soil heat flux, vegetation and soil R_n, respectively. f_{vc} refers to the plant cover fraction.

4. Results

4.1. Evaluation of five individual Ws-based LUE models

To evaluate the simulation performance of the five individual W_s-based LUE model, we detected the response of inversion W_s to six factors (EF, VPD, LSWI, SM, NDVI and LST) (Fig. 4). For all grassland sites, EF showed the highest R^2 (0.70) positively related with the inversion W_s, followed by NDVI and LSWI with R^2 of 0.65 and 0.61, respectively. SM also has positive correlation with R^2 of 0.34. In addition, the inversion W_s shows negative correlations with VPD (R^2 = 0.43) and LST (R^2 = 0.22), respectively. The results indicate that these variables can better characterize the W_s. Deriving from these six factors, the daily GPP estimates of the five individual W_s-based LUE models were directly compared with the corresponding ground measurements at 25 EC flux tower sites. LUE-f_{EF} estimated GPP is the closest to the observations among all models (Fig. 5), implying that LUE-f_{EF} outperforms the other individual W_s-based models with a KGE of 0.44, R^2 of 0.52, bias of 1.3 g C m^{-2} d^{-1} and RMSE of 3.8 g C m^{-2} d^{-1}. The KGE of LUE-f_{LST} is the lowest at 0.15, and the KGEs of the three other individual W_s-based models vary from 0.18 to 0.24. The LUE-f_{VPD} yields the largest bias of 3.9 g C m^{-2} d^{-1}. Other three models yield biases of 3.3 g C m^{-2} d^{-1} for LUE-f_{LSWI}, 2.8 g C m^{-2} d^{-1} for LUE-f_{SM}, and 3.1 g C m^{-2} d^{-1} for LUE-f_{LST}.

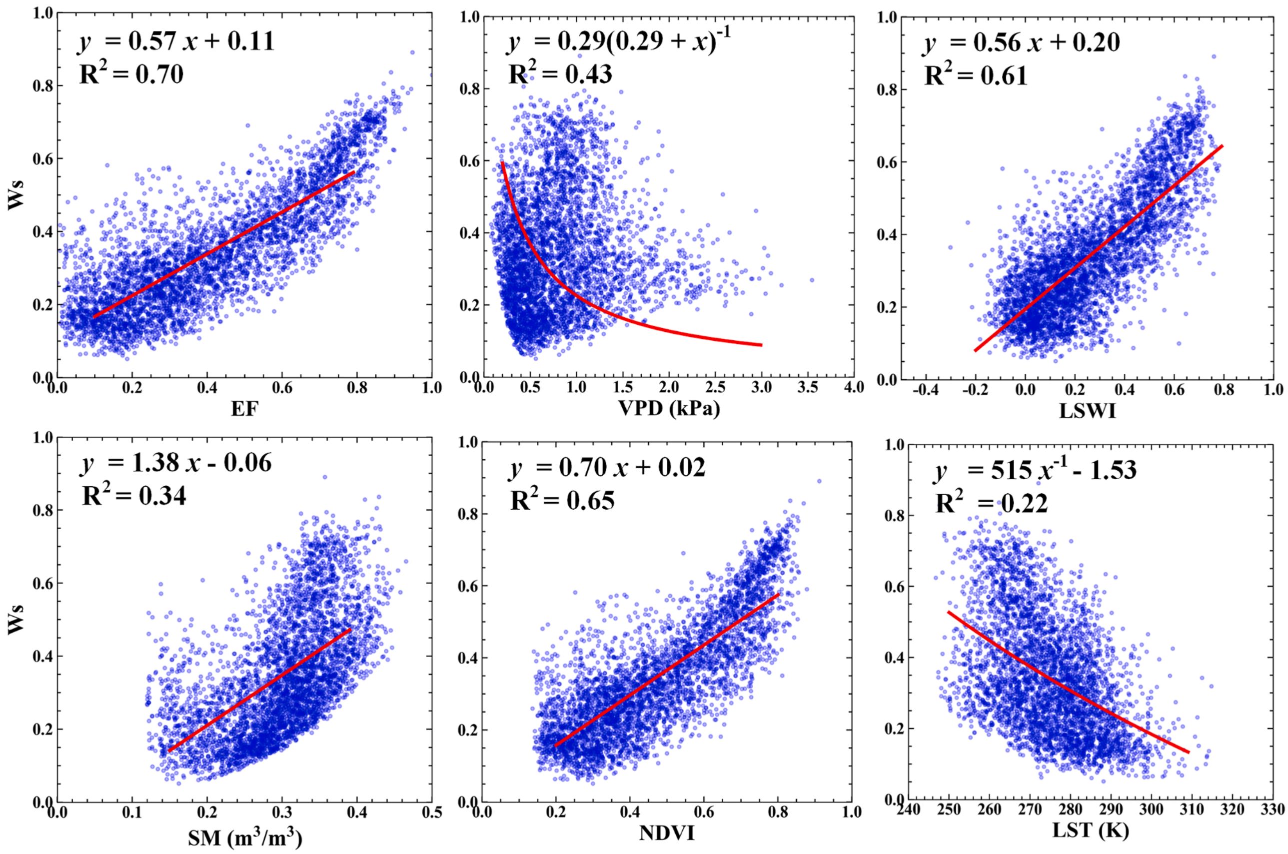

Fig. 4. Scatterplots of inversion W_s and six factors (EF, VPD, LSWI, SM, NDVI and LST). Red lines are the fitted functional curves of inversion W_s to each factor.

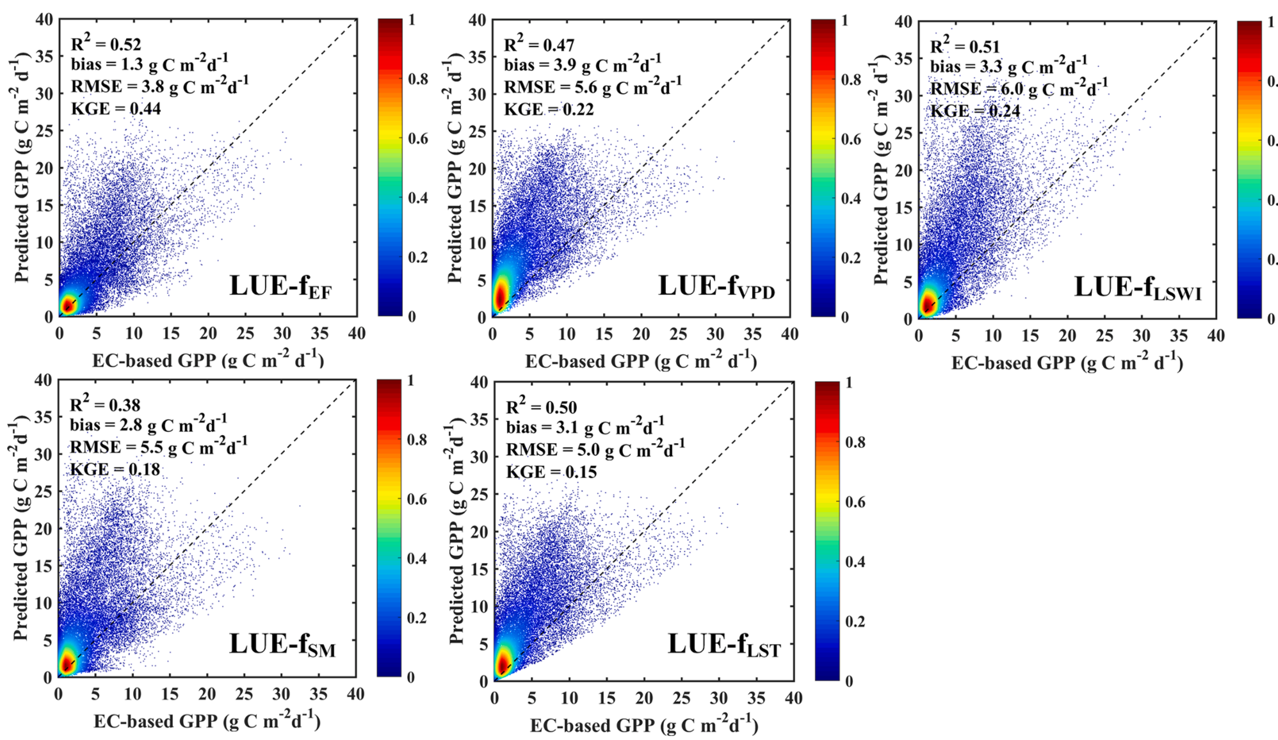

Fig. 5. Scatterplots of daily EC-based and predicted GPP for five individual LUE model (LUE-f_{EF}, LUE-f_{VPD}, LUE-f_{LSWI}, LUE-f_{SM} and LUE-f_{LST}). The color bar represents the density of the scatter increasing from blue to red in range of 0–1.

4.2. Evaluation of LUE-GBRT

The comparison between ground-measured and estimated daily GPP based on leave-one-out cross-validation at all 25 grassland EC sites demonstrates that the estimated daily GPP from LUE-ML is much closer to the EC observations than those of the five individual W_s-based LUE models (Figs. 5 and 6). The KGEs of the estimated versus observed daily GPP for LUE-ML models are all much higher than those of any individual LUE model. The biases of the estimated versus observed daily GPP for LUE-GBRT, LUE-RF, and LUE-ERT are approximately 0 g C m^{-2} d^{-1}, which are lower than those of any individual LUE model. The LUE-GBRT has the highest R^2 (0.88) and KGE (0.85), and the lowest bias and RMSE are 0 and 1.4 g C m^{-2} d^{-1} for the leave-one-out cross-validation, respectively. For daily estimates and observed GPP from the two LUE-ML models (LUE-RF and LUE-ERT), the leave-one-out cross-validations have a similar R^2 (0.75), RMSE (2.0 g C m^{-2} d^{-1}) and bias (0 g C m^{-2} d^{-1}). The KGE of LUE-RF (0.78) is slightly higher than that of LUE-ERT (0.77). The results from the cross-validation indicate that the LUE-GBRT model is stable and has the potential to simulate grassland GPP over the CONUS.

Our evaluation parameter (KGE) between the observed and estimated GPP among LUE-GBRT and the other 10 GPP models at all 25 EC sites indicate that the LUE-GBRT model outperforms the other models, with the highest KGE ranging from 0.28 to 0.90 at all sites (Fig. 7). At the US-ARc site, the LUE-GBRT model performs best (KGE = 0.90). Especially for the US-A32 site, all GPP models illustrate relatively lower performance with KGE (0.01–0.28). In contrast, LUE-GBRT for the US-A32 site has an accuracy of GPP estimates with the highest KGE of 0.28. To further investigate the capacity to simulate GPP, the site-based evaluations indicate that although current GPP estimates from LUE-GBRT model may exhibit biases (Fig. 8), LUE-GBRT estimates appear more accurate on seasonal GPP variations at all sites.

4.3. Mapping of grassland GPP over the CONUS

The amount of grassland GPP increases from spring (MAM) to summer (JJA), and then decreases from the summer (JJA) to winter (DJF). In summer (JJA), the mean GPP is 3.34 g C m^{-2} d^{-1} (Fig. 9). It is much higher than that of spring (MAM, 1.55 g C m^{-2} d^{-1}), fall (SON, 1.43 g C m^{-2} d^{-1}), and winter (DJF, 0.31 g C m^{-2} d^{-1}). For all seasons, the grassland GPP increases from west to east. The multiyear (2019–2021) mean GPP from LUE-GBRT, GBRT, LUE-f_{EF}, LUE-f_{VPD}, LUE-f_{LSWI}, LUE-f_{SM}, and LUE-f_{LST} present consistent spatial patterns over the CONUS (Fig. 10). The annual grassland GPP derived from the all seven models presents obvious increases from the west to the east. Higher GPP was found in central CONUS. Regardless, the seven GPP estimates show discrepancies and high uncertainties (Fig. 10). The domain-average multiyear mean GPP of the seven models ranges from 1.66 to 3.52 g C m^{-2} d^{-1}. The mean estimate of the grassland GPP from LUE-GBRT is 1.66 g C m^{-2} d^{-1}. LUE-f_{EF} GPP is the closest estimate to LUE-GBRT GPP, with an annual average GPP of 1.83 g C m^{-2} d^{-1}. For the LUE-f_{VPD}, GPP estimates are higher than those from other GPP models, with an annual GPP of 3.52 g C m^{-2} d^{-1}.

5. Discussion

5.1. Performance of LUE-GBRT

5.1.1. Capacity for LUE-GBRT to simulate GPP

Water constraints have affected grassland GPP estimates greatly. By integrating multiple water constraints including f_{EF}, f_{VPD}, f_{LSWI}, f_{SM}, and f_{LST}, LUE-GBRT not only yields more accurate and robust grassland GPP estimates with a higher KGE (0.85) than the five individual W_s-based LUE models for all sites (Figs. 5 and 6), but also preserves physical understanding within the LUE model for estimating GPP. These evaluation results at the site scale showed that LUE-GBRT model provides more reliable support for grassland GPP estimates while capturing the seasonal variations effectively. This was mainly because LUE-GBRT model integrated all kinds of water constraints, which better reflecting the effect of water constraints to grassland GPP estimates.

LUE-GBRT model is coupled with multiple water constraints to improve the accuracy of GPP estimates. At all 25 EC sites, the five physical models overestimated the grassland GPP slightly based on the LUE model with a single W_s. Meanwhile, LUE-GBRT better fits the variation in GPP observations by coupling different kinds of water constraints. It presents a superior simulation capacity for capturing temporal features of GPP variations at the site scale. In addition, the annual GPP of LUE-GBRT presents the consistent spatial variation with that of five individual models, which was described by the results of the previous report (Boyte et al., 2017). Substantial previous studies have reported that LUE models had integrated two or more water constraints. For example, Terrestrial Carbon Flux model (TCF) includes VPD and SM to cover the water constraints (He et al., 2016). Joiner and Yoshida (2020) used VPD and SM as the input features of ML method to participate in the prediction of the realized LUE. These LUE models integrating multiple water constraints appeared a better performance than the models that only considered a single W_s, which is consistent with our results. GPP estimates of LUE-GBRT are the multiplication of the absorbed PAR and actual LUE. The actual LUE is downregulated from ε_{max} by environmental conditions, including GBRT-based W_s coupling various water constraints. Therefore, LUE-GBRT, as a hybrid model, not only makes use of the accuracy advantage of ML, but also preserves the physical foundations of the LUE model.

5.1.2. Comparison with pure GBRT

To compare LUE-GBRT and ML approaches, we estimated GPP using the GBRT, as well as RF and ERT model at all 25 sites. The GPP estimates from GBRT, RF, and ERT against EC observations at all sites by leave-

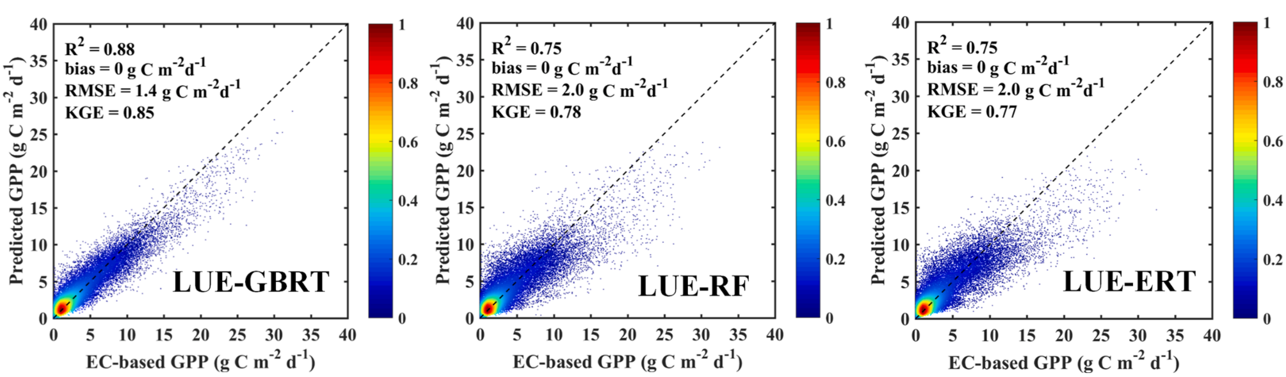

Fig. 6. Scatterplots of EC-based and predicted GPP estimates from three ML-based LUE models (LUE-GBRT, LUE-RF and LUE-ERT) based on the leave-one-out cross-validation. The color bar represents the density of the scatter increasing from blue to red in range of 0–1.

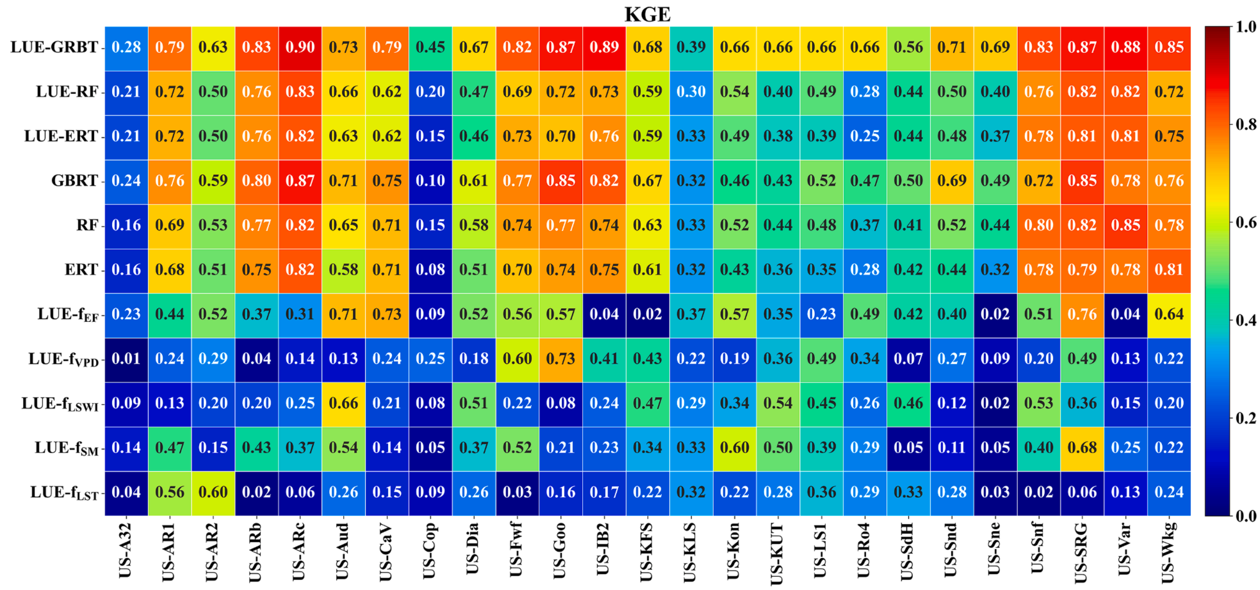

Fig. 7. Diagram of the evaluation parameter (KGE) comparison among 11 GPP models (LUE-GBRT, LUE-RF, LUE-ERT, GBRT, RF, ERT, LUE-f_{EF}, LUE-f_{VPD}, LUE-f_{LSWI}, LUE-f_{SM}, and LUE-f_{LST}) at all 25 EC sites. The color bar represents the values of KGE in range of 0–1, and the numbers are the values of KGE.

one-out cross-validation showed that GBRT yields approximately similar accuracy with the bias of 0 g C m^{-2} d^{-1}, RMSE of 1.4 g C m^{-2} d^{-1}, R^2 of 0.88, and KGE of 0.84 among the ML models (Fig. 11). The accuracy of ERT is slightly lower than that of the other two models. In comparison with GBRT at site scale, the LUE-GBRT has similar accuracy with a KGE of 0.85, an R^2 of 0.88, an RMSE of 1.4 g C m^{-2} d^{-1} and a bias of 0 g C m^{-2} d^{-1} (Fig. 6).

To test the stability and inspect the predictive capacity of extreme events for LUE-ML coupling models, we also compared the accuracy of LUE-GBRT and GBRT in extreme case of low NDVI (Fig. 12). Although LUE-GBRT has an overall similar accuracy with GBRT, in the extreme cases at the low NDVI level ($0 < \mathrm{NDVI} < 0.3$), the LUE-GBRT model outperformed the traditional ML method (i.e., GBRT) under that extreme condition (Fig. 12). For vegetation-sparse cases ($0 < \mathrm{NDVI} < 0.3$), the KGE of GBRT is 0.55, while that of LUE-GBRT is 0.71. The LUE-GBRT increases R^2 of GBRT from 0.61 to 0.81, and decreases the RMSE from 0.7 to 0.5 g C m^{-2} d^{-1}. The results indicate that LUE-GBRT yields better performance than GBRT, emphasizing the capacity of the LUE-GBRT model in simulating GPP in a particular extreme case. In sum, LUE-GBRT not only integrates multiple water constraints but also improves our understanding of GBRT-based W_s in the LUE framework.

We also investigate the spatial difference between the grassland GPP from LUE-GBRT and GBRT (Fig. 13). With sparse vegetation, the difference is larger. Previous studies reported that the pure GBRT method overestimated global grassland GPP with a bias of 0.59 g C m^{-2} d^{-1} (Bai et al., 2021), which is consistent with our results (Fig. 13). This may be attributed to the GBRT structure. Our LUE-GBRT may have better performance on the spatial distribution of grassland GPP over the CONUS.

5.1.3. Impact of input variables on LUE-GBRT

The five water constraints (i.e., f_{EF}, f_{VPD}, f_{LSWI}, f_{SM} and f_{LST}) have different contributions to the LUE-GRBT model determined by SHAP values (Fig. 14). Both f_{EF} and f_{LSWI} are important factors for LUE-GBRT. This may be due to the fact that actual LUE is less sensitive to atmospheric water deficit (e.g., VPD) and soil water indicators (e.g., SM) than to plant water indicators (e.g., EF and LSWI) (Zhang et al., 2015b). f_{EF} is estimated using the ratio of actual LE to R_n because the energy assigned to evaporation leads to a stronger water stress (Chen et al. 2014). The temporal variations of water stress can be captured by LSWI at seasonal scale (Xiao et al., 2004). Additionally, previous studies found that EF, SM and VPD, respectively, explained 36%, 6%, and 20% of LUE monthly variations (Zhang et al., 2015b), which demonstrated that water constraints related to photosynthesis are complicated (Churkina et al., 1999). Therefore, these water constraints contribute to the LUE-GBRT GPP estimates.

Because f_{LST} appears the least important constraint factor in the LUE-GBRT model, can we remove it from LUE-GBRT? Fig. 15 shows the validation of LUE-GBRT GPP estimates coupling four water constraints (f_{EF}, f_{VPD}, f_{SM} and f_{LSWI}) against EC GPP at all 25 sites using leave-one-out cross-validation. By comparing the performance of LUE-GRBT through the five factors (f_{EF}, f_{VPD}, f_{SM}, f_{LSWI} and f_{LST}) (Fig. 6), the R^2 decreases from 0.88 to 0.70, RMSE increases from 1.4 to 2.2 g C m^{-2} d^{-1}, and KGE decreases from 0.85 to 0.76. Overall, although the contribution of f_{LST} to GPP estimates from LUE-GBRT is relatively small, f_{LST} cannot be ignored because of its significant contributions in improving model accuracy. This may be explained by the fact that NDVI and LST are relevant to the ground surface resistance to LE (Jiang and Islam 1999), which are closely related to photosynthesis.

5.2. Uncertainties

LUE-GBRT has advantages on GPP estimation, amid some uncertainties due to model structure, data source and scale mismatches. LUE models abide by LUE logics (Eq. (1)) but have different kinds of structures affecting model performance (Yuan et al. 2014). For example, the LUE component in VPM was the multiplication of ε_{max} and environmental constraints (Xiao et al., 2004), while that of EC-LUE was minimum value of T_s and W_s (Yuan et al. 2007). In addition, we used the inversion W_s as the target variable of GBRT to estimate W_s in the LUE model (Eq. (1)). The structure of the LUE model could influence the calculation of W_s derived from EC-based GPP. In addition, ML models rely more on the *in situ* parameter and EC GPP estimates, which results in overfitting and introduces uncertainties (Yang et al. 2007).

Complex input data sources will introduce uncertainties in LUE-GBRT for GPP estimates. The input datasets in LUE-GBRT include MODIS reflectance, CCI SM, Daymet meteorological reanalysis data, and NLDAS LST data. The accuracies of input datasets could cause large uncertainties (RMSE = 1.6 g C m^{-2} d^{-1}) in GPP estimates (Heinsch et al. 2006). Because there are no long-term, all-weather, high-resolution satellite SM and LST productions over the CONUS available, we only used the bilinear interpolation to downscale the SM and LST, which will lead to large uncertainties in GPP estimates. In addition, validation data

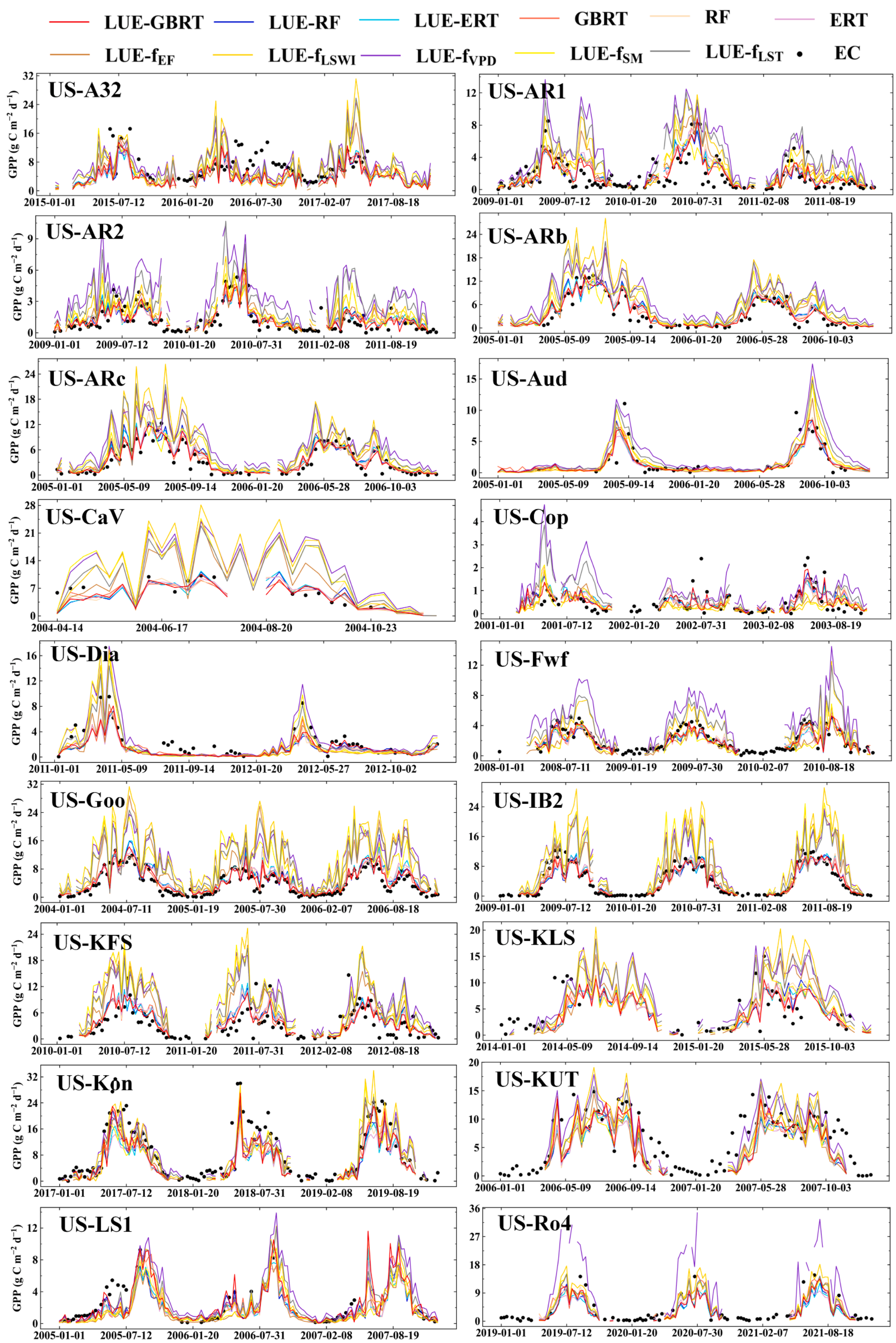

Fig. 8. Temporal variations in estimated and EC GPP from 25 EC sites. The solid lines and black dots represent the GPP estimates of 11 models (LUE-GBRT, LUE-RF, LUE-ERT, GBRT, RF, ERT, LUE-f_{EF}, LUE-f_{VPD}, LUE-f_{LSWI}, LUE-f_{SM}, and LUE-f_{LST}) and EC GPP observations, respectively.

can also lead to some uncertainties. Although EC observations have been broadly accepted as good references for validating GPP estimates, EC GPP also has uncertainties because it is derived from NEE values by nighttime partitioning and gap-filling, which can take 10–30% errors into model accuracy (Reichstein et al. 2005).

The spatial scale mismatch of different datasets is another source of uncertainties in GPP estimation. First, the coarse (e.g., NLDAS LST/CCI SM, 12.5/25 km) and moderate spatial resolution remotely sensed and meteorological reanalysis data (e.g., MODIS reflectance/DAYMET data, 500 m/1 km) have an obvious scale mismatch. Second, the EC

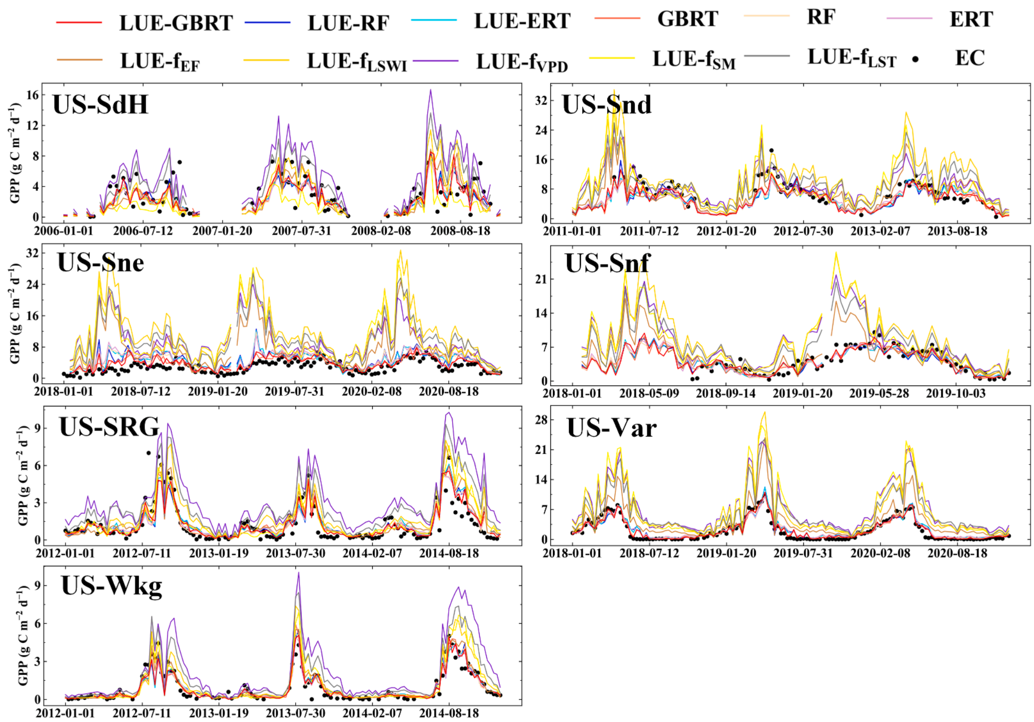

Fig. 8. (*continued*).

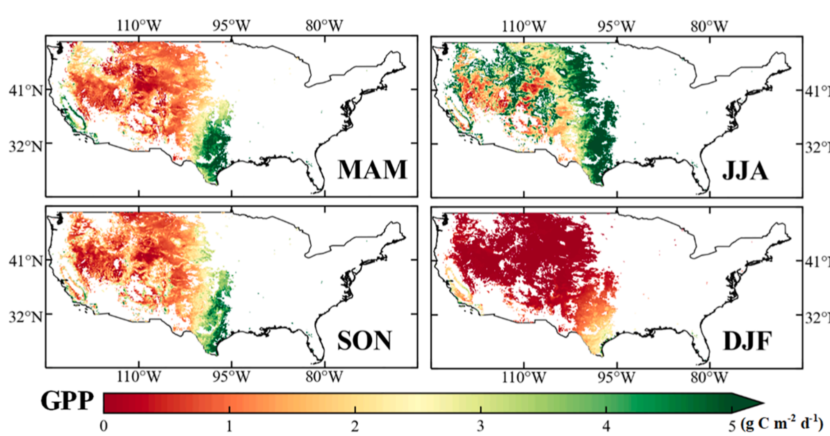

Fig. 9. Seasonal spatial patterns of grassland GPP means for LUE-GBRT over the CONUS during 2019–2021. MAM (March, April, and May) represents spring; JJA (June, July, and August) represents summer; SON (September, October, and November) represents fall; DJF (December, January, and February) represents winter. The color bar represents the values of GPP estimates increasing from red to green.

measurements represent a flux as integration over the EC footprint with a longitudinal length in the scale range from 100 to 2000 m (Baldocchi et al. 2001; Chu et al. 2021; Turner et al. 2003). Third, the scale mismatch also exists between the EC observations and gridded data, which could introduce large uncertainties for estimating GPP.

5.3. Merits and limitations of the LUE-GBRT

Compared to the conventional GPP models, LUE-GBRT has two merits. Compared with individual W_s-based LUE models, LUE-GBRT inherits the generalization ability of ML methods to improve the performance of LUE models and has higher accuracy than individual physical LUE models. Additionally, LUE-GBRT model can improve the accuracy of GPP estimates by coupling different water constraints. This may be attributed to the fact that no indicator is found to explain all the water constraints as much as expected. Compared with ML methods, LUE-GBRT carry a strong physical process on photosynthesis, and outperforms ML method for sparse vegetation. ML methods upscale the EC measurements from site to regional/global scales directly, whereas LUE-GBRT contains a LUE framework that considers GPP as the multiplication of the absorbed PAR and actual LUE. Actual LUE is referred as the efficiency of fixing carbon from absorbed light energy through photosynthesis (Monteith 1972). Our strategy is based on a promising path through coupling the physical constraints and ML methods to estimate GPP.

Nonetheless, LUE-GBRT also has distinct limitations. First, LUE-GBRT framework needs a large number of representative training dataset to estimate W_s in the LUE model. If the samples are not sufficient for a region, LUE-GBRT could result in large biases in GPP estimates. In addition, the quality of samples could affect the accuracy of LUE-GBRT. Second, the assumption of constant ε_{max} may not be very accurate because of the temporal and spatial variability of grassland ε_{max} (Running et al., 2004). Third, LUE-GBRT includes five different W_s which might contain similar information and are highly correlated. For

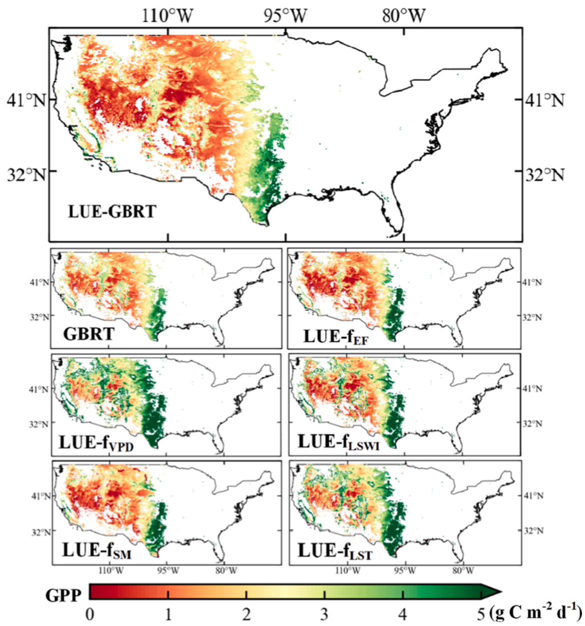

Fig. 10. Maps of average annual grassland GPP during 2019–2021 in the CONUS for LUE-GBRT, GBRT and five individual models (LUE-f_{EF}, LUE-f_{VPD}, LUE-f_{LSWI}, LUE-f_{SM}, and LUE-f_{LST}). The color bar represents the values of GPP estimates increasing from red to green.

example, both LSWI and EF reflect leaf water status (Zhang et al., 2015b). We will explore their differences and select the optimal W_s in the near future. Fourth, because of excluding the saturation of canopy photosynthesis under high incident PAR as suggested by Ibrom et al. (2008), our coupling model might ignore the effect of light saturation from hourly to daily scale and overestimate GPP estimates under clear sky. Finally, we did not distinguish the direct and diffuse radiation in LUE-GBRT. Previous studies found that direct radiation causes a lower LUE than diffuse radiation, which could influence the accuracy of ε_{max} (Wang et al., 2018b).

6. Conclusions

Satellite, hydrological and meteorological data need to be applied to estimate GPP in LUE model through integrating the W_s by GBRT, whose target variable (i.e., inversion W_s) is derived from EC-based GPP. It means this approach can not only be used at point scale, but also for regional simulation. Therefore, we proposed a novel LUE-GBRT framework by coupling a LUE model with an ML-based W_s for estimating grassland GPP over the CONUS. At the site level, LUE-GBRT was superior to all individual W_s-based LUE models, and accurately captured the temporal variations in grassland GPP. LUE-GBRT also performed better than GBRT in the extreme case at sparse vegetation levels. At regional scale, LUE-GBRT also captured the spatial variation of grassland GPP over the CONUS consistent with other models, where GPP estimates increased from the west to the east. We advocate that LUE-GBRT makes ML complementary to the physical-based LUE framework to choose a more suitable junction between GPP physical process and model accuracy.

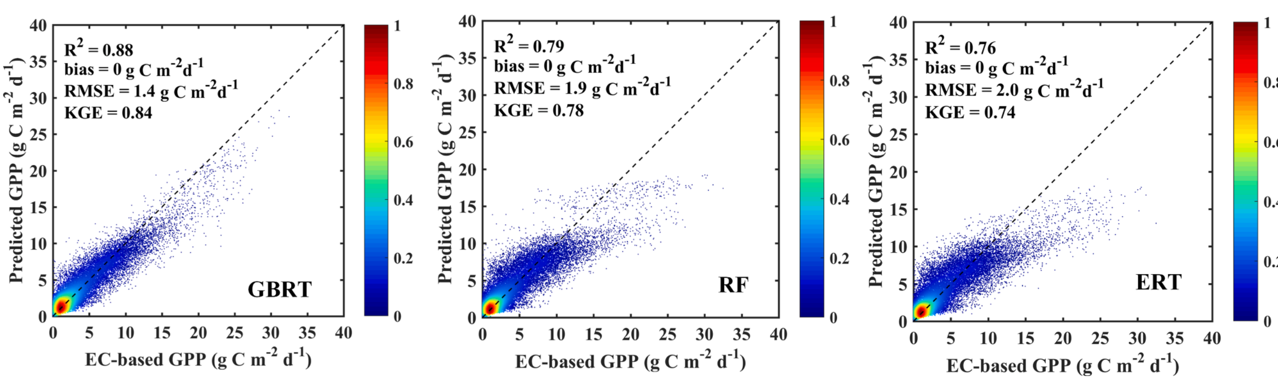

Fig. 11. Scatterplots of daily EC-based and predicted GPP for three pure ML models (GBRT, RF, and ERT) at 25 EC sites using leave-one-out cross-validation. The color bar represents the density of the scatter increasing from blue to red in range of 0–1.

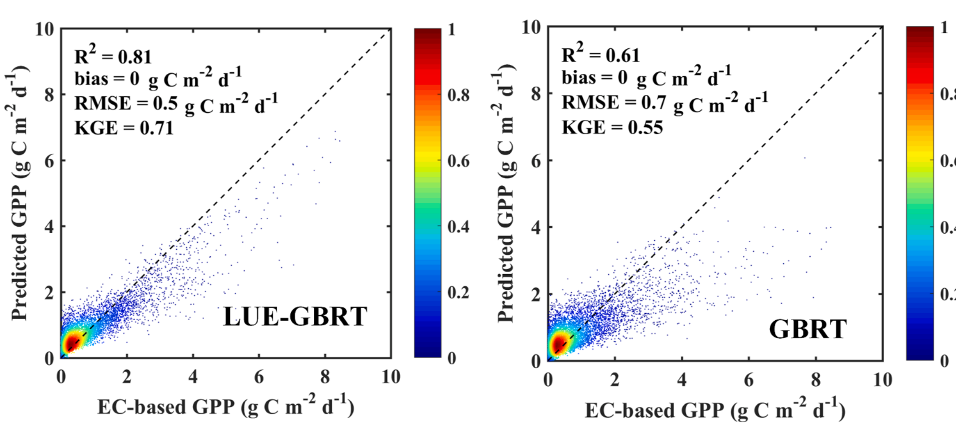

Fig. 12. Scatterplots of daily GPP observations and estimates for LUE-GBRT and pure GBRT in the extreme case of 0 < NDVI < 0.3 at 25 EC sites. The color bar represents the density of the scatter increasing from blue to red in range of 0–1.

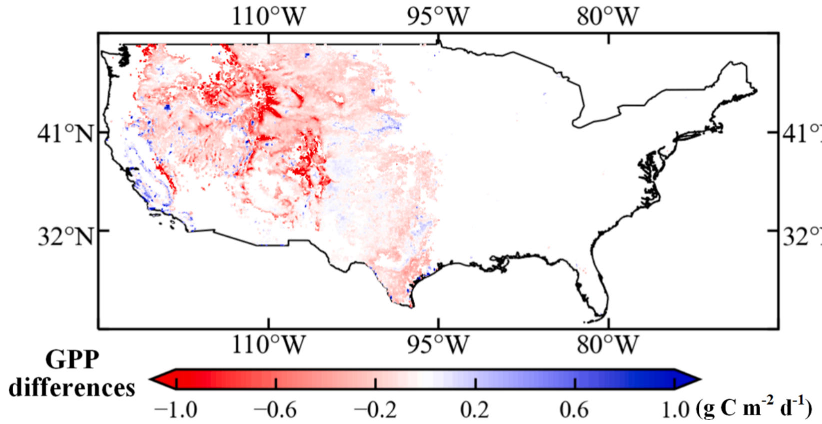

Fig. 13. Map of spatial differences in the average annual grassland GPP over the CONUS during 2019–2021 between LUE-GBRT and GBRT. GPP differences are GPP estimates of LUE-GBRT minus GBRT, increasing from negative (red) to positive (blue) values.

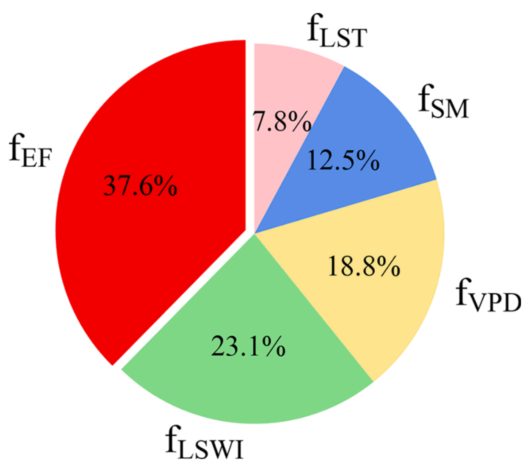

Fig. 14. The contributions of five water constraints (f_{EF}, f_{VPD}, f_{LSWI}, f_{SM} and f_{LST}) to GPP estimates of LUE-GBRT model according to SHAP values. Among the five water constraints, f_{EF} has the most contribution to GPP estimates of LUE-GBRT.

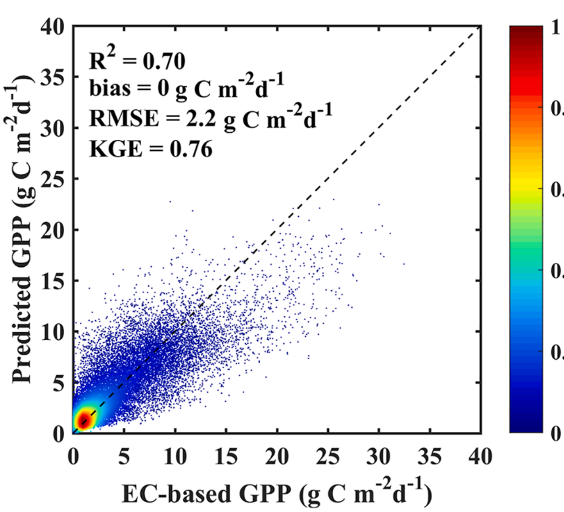

Fig. 15. Scatterplots of EC-based and estimated GPP from LUE-GBRT model coupling four water constraints (f_{EF}, f_{VPD}, f_{LSWI}, and f_{SM}) at 25 EC sites using leave-one-out cross-validation. The color bar represents the density of the scatter increasing from blue to red in range of 0–1.

Declaration of Competing Interest

The authors declare that they have no known competing financial interests or personal relationships that could have appeared to influence the work reported in this paper.

Data availability

The authors do not have permission to share data.

Acknowledgments

This work was supported by the Natural Science Fund of China (No. 42192581, No. 42192580 and No. 42171310). We thank FLUXNET (https://fluxnet.org) and AmeriFlux (https://ameriflux.lbl.gov) for providing EC and meteorological observations. MODIS (https://appeears.earthdatacloud.nasa.gov), ESA CCI SM V07.1 (https://www.esa-soilmoisture-cci.org), DAYMET V4 (https://daac.ornl.gov), and NLDAS NOAH0125_H002 (https://disc.gsfc.nasa.gov) products were obtained online.

Supplementary materials

Supplementary material associated with this article can be found, in the online version, at doi:10.1016/j.agrformet.2023.109634.

References

Adams, J.M., Faure, H., Faure-Denard, L., 1990. Increases in terrestrial carbon storage from the last glacial maximum to the present. Nature 348 (6303), 711–714. https://doi.org/10.1038/348711a0.

Anav, A., et al., 2015. Spatiotemporal patterns of terrestrial gross primary production: a review. Rev. Geophys. 53 (3), 785–818. https://doi.org/10.1002/2015RG000483.

Bai, Y., Liang, S.L., Yuan, W.P., 2021. Estimating global gross primary production from sun-induced chlorophyll fluorescence data and auxiliary information using machine learning methods. Remote Sens. 13 (5), 963. https://doi.org/10.3390/rs13050963.

Baldocchi, D., et al., 2001. FLUXNET: a new tool to study the temporal and spatial variability of ecosystem-scale carbon dioxide, water vapor, and energy flux densities. Bull. Am. Meteorol. Soc. 82 (11), 2415–2434. https://doi.org/10.1175/1520-0477(2001)082<2415:FANTTS>2.3.CO;2.

Bao, S.N., Ibrom, A., Wohlfahrt, G., Koirala, S., Migliavacca, M., Zhang, Q., Carvalhais, N., 2022a. Narrow but robust advantages in two-big-leaf light use efficiency models over big-leaf light use efficiency models at ecosystem level. Agric. For. Meteorol. 326, 109185 https://doi.org/10.1016/j.agrformet.2022.109185.

Bao, S.N., et al., 2022b. Environment-sensitivity functions for gross primary productivity in light use efficiency models. Agric. For. Meteorol. 312, 108708 https://doi.org/10.1016/j.agrformet.2021.108708.

Beck, H.E., Zimmermann, N.E., McVicar, T.R., Vergopolan, N., Berg, A., Wood, E.F., 2020. Present and future Koppen-Geiger climate classification maps at 1-km resolution. Sci. Data 7 (1), 274. https://doi.org/10.1038/s41597-020-00616-w.

Beer, C., et al., 2010. Terrestrial gross carbon dioxide uptake: global distribution and covariation with climate. Science 329 (5993), 834–838. https://doi.org/10.1126/science.1184984.

Boyte, S.P., Wylie, B.K., Howard, D.M., Dahal, D., Gilmanov, T., 2017. Estimating carbon and showing impacts of drought using satellite data in regression-tree models. Int. J. Remote Sens. 39 (2), 374–398. https://doi.org/10.1080/01431161.2017.1384592.

Breiman, L., 2001. Random forests. Mach. Learn. 45 (1), 5–32. https://doi.org/10.1023/A:1010933404324.

Chatterjee, A., Lahiri, S.N., 2011. Bootstrapping Lasso Estimators. J. AM. Stat. Assoc. 106 (494), 608–625. https://doi.org/10.1198/jasa.2011.tm10159.

Chen, D.Y., Huang, J.F., Jackson, T.J., 2005. Vegetation water content estimation for corn and soybeans using spectral indices derived from MODIS near- and short-wave infrared bands. Remote Sens. Environ. 98 (2–3), 225–236. https://doi.org/10.1016/j.rse.2005.07.008.

Chen, J.M., Liu, J., Cihlar, J., Goulden, M.L., 1999. Daily canopy photosynthesis model through temporal and spatial scaling for remote sensing applications. Ecol. Modell. 124 (2–3), 99–119. https://doi.org/10.1016/S0304-3800(99)00156-8.

Chen, J.Q., 2021. Modeling Ecosystem production, Biophysical models and Applications in Ecosystem Analysis. Michigan State University Press, pp. 29–54.

Chen, J.Q., 2023. Unlocking the power of machine learning for Earth system modeling: a game-changing breakthrough. Global Change Biol. 00, 1–3. https://doi.org/10.1111/gcb.16696.

Chen, Y., et al., 2014. Comparison of satellite-based evapotranspiration models over terrestrial ecosystems in China. Remote Sens. Environ. 140, 279–293. https://doi.org/10.1016/j.rse.2013.08.045.

Chu, H.S., et al., 2021. Representativeness of Eddy-Covariance flux footprints for areas surrounding AmeriFlux sites. Agric. For. Meteorol. 301-302, 108350 https://doi.org/10.1016/j.agrformet.2021.108350.

Churkina, G., Running, S.W., Schloss, A.L., Participants Potsdam, N.P.P.M.I., 1999. Comparing global models of terrestrial net primary productivity (NPP): the importance of water availability. Global Change Biol. 5, 46–55. https://doi.org/10.1046/j.1365-2486.1999.00006.x.

Cui, T.X., Wang, Y.J., Sun, R., Qiao, C., Fan, W.J., Jiang, G.Q., Hao, L.Y., Zhang, L., 2016. Estimating vegetation primary production in the Heihe river basin of china with multi-source and multi-scale data. PLoS ONE 11 (4), e0153971. https://doi.org/10.1371/journal.pone.0153971.

[dataset] Dave, B., James, B., Margaret, T., 2019a. AmeriFlux BASE US-AR1 ARM USDA UNL OSU Woodward Switchgrass 1. A. AMP. 3-5. doi:10.17190/AMF/1246137.

[dataset] Dave, B., James, B., Margaret, T., 2019b. AmeriFlux BASE US-AR2 ARM USDA UNL OSU Woodward Switchgrass 2. A. AMP. 3-5. doi:10.17190/AMF/1246138.

[dataset] Dave, B., Lara, K., Margaret, T., Sebastien, B., 2018. AmeriFlux BASE US-A32 ARM-SGP Medford hay pasture. A. AMP. 1-5. doi:10.17190/AMF/1436327.

[dataset] Dave, B., Tim, J.A., 2016. AmeriFlux BASE US-SdH Nebraska SandHills Dry Valley. A. AMP. 1-1. doi:10.17190/AMF/1246136.

[dataset] David, B., 2019. AmeriFlux BASE US-Cop Corral Pocket. A. AMP. 2-5. doi:10.17190/AMF/1246129.

de Almeida, C.T., Delgado, R.C., Galvao, L.S., Aragao, L., Ramos, M.C., 2018. Improvements of the MODIS gross primary productivity model based on a comprehensive uncertainty assessment over the Brazilian Amazonia. ISPRS J. Photogramm. 145, 268–283. https://doi.org/10.1016/j.isprsjprs.2018.07.016.

Dorigo, W., et al., 2017. ESA CCI soil moisture for improved earth system understanding: state-of-the art and future directions. Remote Sens. Environ. 203, 185–215. https://doi.org/10.1016/j.rse.2017.07.001.

Filippi, A.M., Guneralp, I., Randall, J., 2014. Hyperspectral remote sensing of aboveground biomass on a river meander bend using multivariate adaptive regression splines and stochastic gradient boosting. Remote Sens. Lett. 5 (5), 432–441. https://doi.org/10.1080/2150704X.2014.915070.

Fisher, J.B., Tu, K.P., Baldocchi, D.D., 2008. Global estimates of the land-atmosphere water flux based on monthly AVHRR and ISLSCP-II data, validated at 16 FLUXNET sites. Remote Sens. Environ. 112 (3), 901–919. https://doi.org/10.1016/j.rse.2007.06.025.

Friedman, J.H., 2001. Greedy function approximation: a gradient boosting machine. Ann. Stat. 29 (5), 1189–1232. https://doi.org/10.1214/aos/1013203451.

Frouin, R., Pinker, R.T., 1995. Estimating Photosynthetically Active Radiation (PAR) at the earth's surface from satellite observations. Remote Sens. Environ. 51 (1), 98–107. https://doi.org/10.1016/0034-4257(94)00068-X.

Fujimoto, K., Kojadinovic, I.K., Marichal, J.L., 2006. Axiomatic characterizations of probabilistic and cardinal-probabilistic interaction indices. Game Econ. Behav. 55 (1), 72–99. https://doi.org/10.1016/j.geb.2005.03.002.

Gao, Y.N., et al., 2014. A MODIS-based photosynthetic capacity model to estimate gross primary production in Northern China and the Tibetan Plateau. Remote Sens. Environ. 148, 108–118. https://doi.org/10.1016/j.rse.2014.03.006.

Geurts, P., Ernst, D., Wehenkel, L., 2006. Extremely randomized trees. Mach. Learn. 63 (1), 3–42. https://doi.org/10.1007/s10994-006-6226-1.

Gruber, A., Scanlon, T., van der Schalie, R., Wagner, W., Dorigo, W., 2019. Evolution of the ESA CCI soil moisture climate data records and their underlying merging methodology. Earth Syst. Sci. Data 11, 717–739. https://doi.org/10.5194/essd-11-717-2019.

Gupta, H.V., Kling, H., Yilmaz, K.K., Martinez, G.F., 2009. Decomposition of the mean squared error and NSE performance criteria: implications for improving hydrological modelling. J. Hydrol. 377 (1–2), 80–91. https://doi.org/10.1016/j.jhydrol.2009.08.003.

He, M.Z., et al., 2013. Development of a two-leaf light use efficiency model for improving the calculation of terrestrial gross primary productivity. Agr. Forest Meteorol. 173, 28–39. https://doi.org/10.1016/j.agrformet.2013.01.003.

He, M.Z., Kimball, J.S., Running, S., Ballantyne, A., Guan, K.Y., Huemmrich, F., 2016. Satellite detection of soil moisture related water stress impacts on ecosystem productivity using the MODIS-based photochemical reflectance index. Remote Sens. Environ. 186, 173–183. https://doi.org/10.1016/j.rse.2016.08.019.

Heinsch, F.A., et al., 2006. Evaluation of remote sensing based terrestrial productivity from MODIS using regional tower eddy flux network observations. IEEE T Geosci. Remote Sens. 44 (7), 1908–1925. https://doi.org/10.1109/TGRS.2005.853936.

Horn, J.E., Schulz, K., 2011. Identification of a general light use efficiency model for gross primary production. Biogeosciences 8 (4), 999–1021. https://doi.org/10.5194/bg-8-999-2011.

Ibrom, A., Oltchev, A., June, T., Kreilein, H., Rakkibu, G., Ross, T., Panferov, O., Gravenhorst, G., 2008. Variation in photosynthetic light-use efficiency in a mountainous tropical rain forest in Indonesia. Tree Physiol. 28 (4), 499–508. https://doi.org/10.1093/treephys/28.4.499.

Jiang, B., et al., 2015. Empirical estimation of daytime net radiation from shortwave radiation and ancillary information. Agr. Forest Meteorol. 211-212, 23–36. https://doi.org/10.1016/j.agrformet.2015.05.003.

Jiang, L., Islam, S., 1999. A methodology for estimation of surface evapotranspiration over large areas using remote sensing observation. Geophys. Res. Lett. 26, 2773–2776. https://doi.org/10.1029/1999GL006049.

Jin, Y.F., Randerson, J.T., Goulden, M.L., 2011. Continental-scale net radiation and evapotranspiration estimated using MODIS satellite observations. Remote Sens. Environ. 115 (9), 2302–2319. https://doi.org/10.1016/j.rse.2011.04.031.

[dataset] Joe, M., 2016. AmeriFlux BASE US-KUT KUOM Turfgrass Field. A. AMP. 1-1. doi:10.17190/AMF/1246145.

[dataset] John, B., Tim, G., 2022. AmeriFlux BASE US-Ro4 Rosemount Prairie. A. AMP. 15-5. doi:10.17190/AMF/1419507.

Joiner, J., Yoshida, Y., 2020. Satellite-based reflectances capture large fraction of variability in global gross primary production (GPP) at weekly time scales. Agr. Forest Meteorol. 291, 108092 https://doi.org/10.1016/j.agrformet.2020.108092.

Jung, M., Reichstein, M., Bondeau, A., 2009. Towards global empirical upscaling of FLUXNET eddy covariance observations: validation of a model tree ensemble approach using a biosphere model. Biogeosciences 6 (10), 2001–2013. https://doi.org/10.5194/bg-6-2001-2009.

Kalliokoski, T., Mäkelä, A., Fronzek, S., Minunno, F., Peltoniemi, M., 2018. Decomposing sources of uncertainty in climate change projections of boreal forest primary production. Agric. For. Meteorol. 262, 192–205. https://doi.org/10.1016/j.agrformet.2018.06.030.

Karlson, R.H., Cornell, H.V., Hughes, T.P., 2004. Coral communities are regionally enriched along an oceanic biodiversity gradient. Nature 429 (6994), 867–870. https://doi.org/10.1038/nature02685.

[dataset] Kuno, K., Camilo, R.S., Daphne, S., Dennis, B., 2020. AmeriFlux BASE US-Snf Sherman Barn. A. AMP. 3-5. doi:10.17190/AMF/1579718.

Landsberg, J.J., Waring, R.H., 1997. A generalised model of forest productivity using simplified concepts of radiation-use efficiency, carbon balance and partitioning. For. Ecol. Manage. 95 (3), 209–228. https://doi.org/10.1016/S0378-1127(97)00026-1.

Lewis, J.M., 1995. The story behind the Bowen ratio. Bull. Am. Meteorol. Soc. 76 (12), 2433–2443. https://doi.org/10.1175/1520-0477(1995)076<2433:TSBTBR>2.0.CO;2.

Liang, S.L., 2001. Narrowband to broadband conversions of land surface albedo I Algorithms. Remote Sens. Environ. 76 (2), 213–238. https://doi.org/10.1016/S0034-4257(00)00205-4.

Lipovetsky, S., Conklin, M., 2001. Analysis of regression in game theory approach. Appl. Stoch. Model Bus. 17 (4), 319–330. https://doi.org/10.1002/asmb.446.

Lundberg, S., Erion, G.G., Lee, S., 2018. Consistent individualized feature attribution for tree ensembles. arXiv: Learning.

[dataset] Ma, S.Y., Xu, L.K., Verfaillie, J., Baldocchi, D., 2022. AmeriFlux BASE US-Var Vaira Ranch- Ione. A. AMP. 17-5. doi:10.17190/AMF/1245984.

MÄKelÄ, A., et al., 2008. Developing an empirical model of stand GPP with the LUE approach: analysis of eddy covariance data at five contrasting conifer sites in Europe. Global Change Biol. 14 (1), 92–108. https://doi.org/10.1111/j.1365-2486.2007.01463.x.

[dataset] Margaret, T., 2019a. AmeriFlux BASE US-ARb ARM Southern Great Plains burn site- Lamont. A. AMP. 3-5. doi:10.17190/AMF/1246025.

[dataset] Margaret, T., 2019b. AmeriFlux BASE US-ARc ARM Southern Great Plains control site-Lamont. A. AMP. 3-5. doi:10.17190/AMF/1246026.

[dataset] Matteo, D., Cove, S., Patty, O., Joseph, V., Dennis, B., 2016. AmeriFlux BASE US-Snd Sherman Island. A. AMP. 2-1. doi:10.17190/AMF/1246094.

Monteith, J.L., 1972. Solar-radiation and productivity in tropical ecosystems. J Appl. Ecol. 9 (3), 747–766. https://doi.org/10.2307/2401901.

Myneni, R.B., Williams, D.L., 1994. On the relationship between FPAR and NDVI. Remote Sens. Environ. 49 (3), 200–211. https://doi.org/10.1016/0034-4257(94)90016-7.

[dataset] Nathaniel, B., 2020a. AmeriFlux BASE US-KFS Kansas Field Station. A. AMP. 7-5. doi:10.17190/AMF/1246132.

[dataset] Nathaniel, B., 2020b. AmeriFlux BASE US-Kon Konza Prairie LTER (KNZ). A. AMP. 5-5. doi:10.17190/AMF/1246068.

[dataset] Nathaniel, B., 2021. AmeriFlux BASE US-KLS Kansas Land Institute. A. AMP. 2-5. doi:10.17190/AMF/1498745.

Norman, J.M., Perry, S.G., Fraser, A.B., Mach, W., 1978. Remote sensing of canopy architecture. B Am. Meteorol. Soc. 59 (11), 1513. -1513.

Odum, E.P., Kuenzler, E.J., Blunt, M.X., 1958. Uptake of P-32 and primary productivity in marine benthic algae. Limnol. Oceanogr. 3 (3), 340–345. https://doi.org/10.4319/lo.1958.3.3.0340.

Potter, C.S., Randerson, J.T., Field, C.B., Matson, P.A., Vitousek, P.M., Mooney, H.A., Klooster, S.A., 1993. Terrestrial ecosystem production: a process model based on

global satellite and surface data. Global Biogeochem. Cy. 7, 811–841. https://doi.org/10.1029/93GB02725.
Prince, S.D., Goward, S.N., 1995. Global primary production: a remote sensing approach. J. Biogeogr. 22 (4–5), 815–835. https://doi.org/10.2307/2845983.
Purdy, A.J., Fisher, J.B., Goulden, M.L., Colliander, A., Halverson, G., Tu, K., Famiglietti, J.S., 2018. SMAP soil moisture improves global evapotranspiration. Remote Sens. Environ. 219, 1–14. https://doi.org/10.1016/j.rse.2018.09.023.
Raich, J.W., Rastetter, E.B., Melillo, J.M., Kicklighter, D.W., Steudler, P.A., Peterson, B. J., Grace, A.L., Moore Iii, B., Vorosmarty, C.J., 1991. Potential net primary productivity in South America: application of a global model. Ecol. Appl. 1 (4), 399–429. https://doi.org/10.2307/1941899.
Reichstein, M., et al., 2005. On the separation of net ecosystem exchange into assimilation and ecosystem respiration: review and improved algorithm. Global Change Biol. 11 (9), 1424–1439. https://doi.org/10.1111/j.1365-2486.2005.001002.x.
Reichstein, M., et al., 2003. Inverse modeling of seasonal drought effects on canopy CO_2/H_2O exchange in three Mediterranean ecosystems. J. Geophys. Res. 108 (D23) https://doi.org/10.1029/2003JD003430.
Reichstein, M., et al., 2002a. Severe drought effects on ecosystem CO_2 and H_2O fluxes at three Mediterranean evergreen sites: revision of current hypotheses? Global Change Biol. 8 (10), 999–1017. https://doi.org/10.1046/j.1365-2486.2002.00530.x.
Reichstein, M., Tenhunen, J.D., Roupsard, O., Ourcival, J.M., Rambal, S., Dore, S., Valentini, R., 2002b. Ecosystem respiration in two Mediterranean evergreen Holm Oak forests: drought effects and decomposition dynamics. Functional Ecol. 16 (1), 27–39. https://doi.org/10.1046/j.0269-8463.2001.00597.x.
[dataset] Robert, S., Kyle, H., Daphne, S., Joseph, V., Dennis, B., 2021. AmeriFlux BASE US-Sne Sherman Island Restored Wetland. A. AMP. 7-5. doi:10.17190/AMF/1418684.
[dataset] Roser, M., 2019. AmeriFlux BASE US-IB2 Fermi National Accelerator Laboratory-Batavia (Prairie site). A. AMP .8-5. doi:10.17190/AMF/1246066.
Running, S.W., Nemani, R.R., Heinsch, F.A., Zhao, M.S., Reeves, M., Hashimoto, H., 2004. A continuous satellite-derived measure of global terrestrial primary production. Biogeosciences 54 (6), 547–560. https://doi.org/10.1641/0006-3568(2004)054[0547:ACSMOG]2.0.CO;2.
Running, S.W., Thornton, P.E., Nemani, R., Glassy, J.M., 2000. Global terrestrial gross and net primary productivity from the earth observing system. Methods in Ecosystem Science. Springer-Verlag, New York, pp. 44–57.
[dataset] Russell, S., 2020. AmeriFlux BASE US-LS1 San Pedro River Lewis Springs Sacaton Grassland. A. AMP. 1-5. doi:10.17190/AMF/1660346.
[dataset] Russell, S., 2023a. AmeriFlux BASE US-SRG Santa Rita Grassland. A. AMP. 14-5. doi:10.17190/AMF/1246154.
[dataset] Russell, S., 2023b. AmeriFlux FLUXNET-1F US-Wkg Walnut Gulch Kendall Grasslands. A. AMP. 3-5. doi:10.17190/AMF/1984575.
Ryu, Y., et al., 2011. Integration of MODIS land and atmosphere products with a coupled-process model to estimate gross primary productivity and evapotranspiration from 1km to global scales. Global Biogeochem. Cycles 25, GB4017. https://doi.org/10.1029/2011GB004053.
[dataset] Sabina, D., Thomas, K., 2019. AmeriFlux BASE US-Fwf Flagstaff - Wildfire. A. AMP. 8-5. doi:10.17190/AMF/1246052.
[dataset] Shangguan, W., Dai, Y.J., 2014. The global soil dataset for earth system modeling (2014). A Big Earth Data Platform for Three Poles. 10.11888/Soil.tpdc.270578. https://cstr.cn/18406.11.Soil.tpdc.270578.
Shangguan, W., Dai, Y.J., Duan, Q.Y., Liu, B.Y., Yuan, H., 2014. A global soil data set for earth system modeling. J. Adv. Model Earth Syst. 6 (1), 249–263. https://doi.org/10.1002/2013MS000293.
[dataset] Sonia, W., 2016. AmeriFlux BASE US-Dia Diablo. A. AMP. 1-1. doi:10.17190/AMF/1246146.
Stocker, B.D., Wang, H., Smith, N.G., Harrison, S.P., Keenan, T.F., Sandoval, D., Davis, T., Prentice, I.C., 2020. P-model v1.0: an optimality-based light use efficiency model for simulating ecosystem gross primary production. Geosci. Model Dev. 13 (3), 1545–1581. https://doi.org/10.5194/gmd-13-1545-2020.
Stocker, B.D., Zscheischler, J., Keenan, T.F., Prentice, I.C., Seneviratne, S.I., Peñuelas, J., 2019. Drought impacts on terrestrial primary production underestimated by satellite monitoring. Nat. Geosci. 12 (4), 264–270. https://doi.org/10.1038/s41561-019-0318-6.
[dataset] Thornton, M.M.R., Shrestha, Y., Wei, P.E., Thornton, S.K., Wilson, B.E., 2020. Daymet: Daily Surface Weather Data On a 1-km Grid for North America, Version 4. O. DAAC, Oak Ridge, Tennessee, USA. https://doi.org/10.3334/ORNLDAAC/1840.
[dataset] Tilden, M., 2016a. AmeriFlux BASE US-Aud Audubon Research Ranch. A. AMP. 1-4. doi:10.17190/AMF/1246028.
[dataset] Tilden, M., 2016b. AmeriFlux BASE US-CaV Canaan Valley. A. AMP. 2-1. doi:10.17190/AMF/1246042.
[dataset] Tilden, M., 2019. AmeriFlux BASE US-Goo Goodwin Creek. A.AMP. 3-5. doi:10.17190/AMF/1246058.
Townshend, J.R.G., Goff, T.E., Tucker, C.J., 1985. Multitemporal dimensionality of images of normalized difference vegetation index at continental scales. IEEE T Geosci. Remote 23 (6), 888–895. https://doi.org/10.1109/TGRS.1985.289474.
Tramontana, G., et al., 2016. Predicting carbon dioxide and energy fluxes across global FLUXNET sites with regression algorithms. Biogeosciences 13 (14), 4291–4313. https://doi.org/10.5194/bg-13-4291-2016.
Turner, D.P., et al., 2003. Scaling Gross Primary Production (GPP) over boreal and deciduous forest landscapes in support of MODIS GPP product validation. Remote Sens. Environ. 88 (3), 256–270. https://doi.org/10.1016/j.rse.2003.06.005.
Turner, D.P., Ritts, W.D., Styles, J.M., Yang, Z., Cohen, W.B., Law, B.E., Thornton, P.E., 2006. A diagnostic carbon flux model to monitor the effects of disturbance and interannual variation in climate on regional NEP. Tellus. B. 58 (5), 476–490. https://doi.org/10.1111/j.1600-0889.2006.00221.x.
Verrelst, J., van der Tol, C., Magnani, F., Sabater, N., Rivera, J.P., Mohammed, G., Moreno, J., 2016. Evaluating the predictive power of sun-induced chlorophyll fluorescence to estimate net photosynthesis of vegetation canopies: a SCOPE modeling study. Remote Sens. Environ. 176, 139–151. https://doi.org/10.1016/j.rse.2016.01.018.
Wang, S., Ibrom, A., Bauer-Gottwein, P., Garcia, M., 2018a. Incorporating diffuse radiation into a light use efficiency and evapotranspiration model: an 11-year study in a high latitude deciduous forest. Agr. Forest Meteorol. 248, 479–493. https://doi.org/10.1016/j.agrformet.2017.10.023.
Wang, S., Ibrom, A., Bauer-Gottwein, P., Garcia, M., 2018b. Incorporating diffuse radiation into a light use efficiency and evapotranspiration model: an 11-year study in a high latitude deciduous forest. Agric. For. Meteorol. 248, 479–493. https://doi.org/10.1016/j.agrformet.2017.10.023.
Wang, S.Q., et al., 2015. Improving the light use efficiency model for simulating terrestrial vegetation gross primary production by the inclusion of diffuse radiation across ecosystems in China. Ecol. Complex 23, 1–13. https://doi.org/10.1016/j.ecocom.2015.04.004.
Wei, S.H., Yi, C.X., Fang, W., Hendrey, G., 2017. A global study of GPP focusing on light-use efficiency in a random forest regression model. Ecosphere 8 (5), e01724. https://doi.org/10.1002/ecs2.1724.
Wu, X.C., et al., 2015. Performance of linear and nonlinear two-leaf light use efficiency models at different temporal scales. Remote Sens. 7 (3), 2238–2278. https://doi.org/10.3390/rs70302238.
Xia, Y.L., et al., 2012. Continental-scale water and energy flux analysis and validation for the North American Land Data Assimilation System project phase 2 (NLDAS-2): 1. Intercomparison and application of model products. J. Geophys. Res. 117, D03109. https://doi.org/10.1029/2011JD016048.
Xiao, J.F., et al., 2010. A continuous measure of gross primary production for the conterminous United States derived from MODIS and AmeriFlux data. Remote Sens. Environ. 114 (3), 576–591. https://doi.org/10.1016/j.rse.2009.10.013.
Xiao, X.M., Hollinger, D., Aber, J., Goltz, M., Davidson, E.A., Zhang, Q.Y., Moore, B., 2004. Satellite-based modeling of gross primary production in an evergreen needleleaf forest. Remote Sens. Environ. 89 (4), 519–534. https://doi.org/10.1016/j.rse.2003.11.008.
Xu, T.R., et al., 2018. Evaluating Diffferent Machine Learning Methods for Upscaling Evapotranspiration from Flux Towers to the Regional Scale. J. Geophys. Res-Atmos. 123 (16), 8674–8690. https://doi.org/10.1029/2018JD028447.
Yan, H., et al., 2015. Improved global simulations of gross primary product based on a new definition of water stress factor and a separate treatment of C3 and C4 plants. Ecol. Model. 297, 42–59. https://doi.org/10.1016/j.ecolmodel.2014.11.002.
Yan, H., et al., 2017. A novel diffuse fraction-based two-leaf light use efficiency model: an application quantifying photosynthetic seasonality across 20 AmeriFlux flux tower sites. J. Adv. Model. Earth SY 9 (6), 2317–2332. https://doi.org/10.1002/2016MS000886.
Yang, F.H., et al., 2007. Developing a continental-scale measure of gross primary production by combining MODIS and AmeriFlux data through Support Vector Machine approach. Remote Sens. Environ. 110 (1), 109–122. https://doi.org/10.1016/j.rse.2007.02.016.
Yao, Y.J., et al., 2013. MODIS-driven estimation of terrestrial latent heat flux in China based on a modified Priestley–Taylor algorithm. Agr. Forest Meteorol. 171-172, 187–202. https://doi.org/10.1016/j.agrformet.2012.11.016.
Yuan, W.P., et al., 2014. Global comparison of light use efficiency models for simulating terrestrial vegetation gross primary production based on the LaThuile database. Agr. Forest Meteorol. 192-193, 108–120. https://doi.org/10.1016/j.agrformet.2014.03.007.
Yuan, W.P., et al., 2010. Global estimates of evapotranspiration and gross primary production based on MODIS and global meteorology data. Remote Sens. Environ. 114 (7), 1416–1431. https://doi.org/10.1016/j.rse.2010.01.022.
Yuan, W.P., et al., 2007. Deriving a light use efficiency model from eddy covariance flux data for predicting daily gross primary production across biomes. Agr. Forest Meteorol. 143 (3–4), 189–207. https://doi.org/10.1016/j.agrformet.2006.12.001.
Yuan, W.P., et al., 2019. Increased atmospheric vapor pressure deficit reduces global vegetation growth. Sci. Adv. 5 (8), eaax1396 https://doi.org/10.1126/sciadv.aax1396.
Zhang, L.L., Marshall, M., Nelson, A., Vrieling, A., 2021. A global assessment of PT-JPL soil evaporation in agroecosystems with optical, thermal, and microwave satellite data. Agr. Forest Meteorol. 306, 108455 https://doi.org/10.1016/j.agrformet.2021.108455.
Zhang, L.X., Zhou, D.C., Fan, J.W., Hu, Z.M., 2015a. Comparison of four light use efficiency models for estimating terrestrial gross primary production. Ecol. Modell. 300, 30–39. https://doi.org/10.1016/j.ecolmodel.2015.01.001.
Zhang, Y.L., Song, C.H., Sun, G., Band, L.E., McNulty, S., Noormets, A., Zhang, Q.F., Zhang, Z.Q., 2016. Development of a coupled carbon and water model for estimating global gross primary productivity and evapotranspiration based on eddy flux and remote sensing data. Agr. Forest Meteorol. 223, 116–131. https://doi.org/10.1016/j.agrformet.2016.04.003.
Zhang, Y.L., Song, C.H., Sun, G., Band, L.E., Noormets, A., Zhang, Q.F., 2015b. Understanding moisture stress on light use efficiency across terrestrial ecosystems

based on global flux and remote-sensing data. J Geophys. Res-Biogeo. 120 (10), 2053–2066. https://doi.org/10.1002/2015JG003023.
Zhang, Y.Q., Kong, D.D., Gan, R., Chiew, F.H.S., McVicar, T.R., Zhang, Q., Yang, Y.T., 2019. Coupled estimation of 500m and 8-day resolution global evapotranspiration and gross primary production in 2002-2017. Remote Sens. Environ. 222, 165–182. https://doi.org/10.1016/j.rse.2018.12.031.
UCMP, 2022. UC Museum of Paleontology: the grassland biome. https://ucmp.berkeley.edu/exhibits/biomes/grasslands.php (accessed 23 June 2023).